UTILIZATION OF PIEZOELECTRIC EFFECT IN ZINC OXIDE NANOWIRES AS A NANOGENERATOR

by

MOHAMAD HASAN ALEINAWI

A thesis submitted to the Graduate School of Engineering and Natural Science in partial fulfillment of the requirements for the degree of Master of Science

Sabanci University

June 2022

ABSTRACT

UTILIZATION OF PIEZOELECTRIC EFFECT IN ZINC OXIDE NANOWIRES AS A NANOGENERATOR

Mohamad Hasan Aleinawi

Supervisor: Assoc. Prof. Dr. Emre Erdem

Keywords: Zinc oxide nanowires, piezoelectric properties, intrinsic and extrinsic point defects, spectroscopy, ball milling, hydrothermal technique.

Zinc oxide (ZnO) holds a special stature in materials for energy applications due to its phenomenal properties. The wide range of ZnO morphologies enables a wide range of applications such as nanogenerators, sensors, dilute magnetic semiconductors (DMS), light-emitting diodes (LED), and many others. Synthesis techniques of high aspect ratio ZnO nanowires (NW) have been thoroughly studied in the past decade for high piezoelectric properties products. This thesis provides an addition to the vast research of ZnO NWs synthesis by the microwave-assisted hydrothermal method owing to its advantages of high-quality NWs product, simplicity, and rapidness. ZnO NWs synthesized by the microwave-assisted method are analyzed by spectroscopic techniques to gain an understanding of the defective structure of ZnO. The intrinsic and extrinsic defective structure of ZnO NWs is analyzed by electron paramagnetic resonance (EPR) spectroscopy, introduced into the structure by the controlled manipulation of the nano-structure, or doping with transition metal ions (TMI) such as Mn. The outcome is optimizing the process of producing ZnO NWs with a high piezoelectric coefficient up to 20 pC/N.

ÖZET

NANOJENERATÖR OLARAK ÇİNKO OKSİT NANOTELLERİNDE PIEZOELEKTRİK ETKİNİN KULLANILMASI

Mohamad Hasan Aleinawi

Danışman: Doç. Dr. Emre Erdem

Anahtar Kelimeler: Çinko oksit nanoteller, piezoelektrik özellikler, içsel ve dışsal nokta kusurları, spektroskopi, bilyalı öğütme, hidrotermal teknik..

Çinko oksit (ZnO), olağanüstü özellikleri nedeniyle enerji uygulamaları için malzemelerde özel bir yere sahiptir. Geniş ZnO morfolojisi yelpazesi, nanojeneratörler, sensörler, seyreltik manyetik yarı iletkenler (DMS), ışık yayan diyotlar (LED) ve diğerleri gibi çok çeşitli uygulamalara olanak tanır. Yüksek en-boy oranlı ZnO nanotellerinin (NW) sentez teknikleri, yüksek piezoelektrik özelliklere sahip ürünler için son on yılda kapsamlı bir şekilde incelenmiştir. Bu tez, yüksek kaliteli NWs ürünü, basitliği ve hızı avantajlarından dolayı mikrodalga destekli hidrotermal yöntemle ZnO NWs sentezinin geniş araştırmasına bir ek sağlar. Mikrodalga destekli yöntemle sentezlenen ZnO NW'ler, ZnO'nun kusurlu yapısının anlaşılmasını sağlamak için spektroskopik tekniklerle analiz edilir. ZnO NW'lerin içsel ve dışsal kusurlu yapısı, nanoyapının kontrollü manipülasyonu veya Mn gibi geçiş metal iyonları (TMI) ile doping yoluyla yapıya eklenen elektron paramanyetik rezonans (EPR) spektroskopisi ile analiz edilir. Sonuç, 20 pC/N'ye kadar yüksek bir piezoelektrik katsayısı ile ZnO NW'lerin üretim sürecini optimize eder.

Acknowledgment

It has been a blessing to study and work at Sabanci University and to be a member of such a lovely community. This journey enabled me to push myself to my very limit, and be the best version of myself to have the ability to make a humble contribution befitting to this blessing.

First of all, words can not express my gratitude and appreciation for my supervisor, mentor, and role model Assoc. Prof. Dr. Emre Erdem for his unlimited support and kindness. As a sun illuminating the darkest of nights, you enlightened our minds with your vast knowledge and helped me grow and achieve things I have never thought I could achieve.

I would like to express my sincerest gratitude to all the professors who shared their vast knowledge with us and taught us to pursue research with decency and integrity. I would like to also thank all the heroes who kept us safe and helped keep the research running during the difficult times of the pandemic. Huge thanks to the esteemed jury members Assoc. Prof. Dr. Feray Bakan, and Prof. Dr. Mehmet Sankır for their valuable time reviewing and evaluating my work.

Last but not least, my deepest thanks and appreciation to my colleagues Merve Buldu, Ameenuddin Ammar, Ipek Deniz, and Sumaiyah Najib for the lovely times and unforgettable memories we shared during our work.

Finally, I am extremely thankful to my family and friends for their support. Separated by distance, but our hearts are in the same place.

Table of Content

List of Figures

List of Tables

1. Introduction

The demand for clean sources of energy has been the main focus for the majority of researchers in the past decade. Motivated by the vision of the International Energy Agency (IEA) of achieving zero carbon emission by 2050, a global movement for clean energy sources has been initiated [1]. Among materials for clean energy, Zinc Oxide (ZnO) holds a special stature due to its phenomenal properties. ZnO can be synthesized by many facile methods including hydrothermal, co-precipitation, sol-gel, and lots of other methods, and its morphology can be controlled easily by selecting the optimum synthesis method. ZnO nanowires (NWs) have a valuable piezoelectric property, and it is bio-safe and non-toxic, which makes them a great candidate for many applications. Thus, NWs morphology will be in the main scope of this thesis. Some biomedical devices and sensors require sustainable sources of energy. It would be troublesome if these systems required an outer source of energy to work. Moreover, bio-safe and efficient sources of energy are a must for such devices. The most convenient solution for the aforementioned concerns is using "nanogenerators". Nanogenerators (NGs) are devices with the ability to harvest electrical energy from different abundant sources, such as mechanical and thermal sources.

The idea of harvesting energy is not new by itself, it goes back to the end of the 17th century. The first form of energy harvesting started in 1663 with the first primitive friction machine. Then in 1883 electromagnetic generators were discovered, and are still used up to this day. Later in 1929 the Van de Graaf generator was invented. It could produce a high-voltage direct current. Technology kept on evolving up to finally developing the first NG. Different types of NGs will be discussed further in the state of art section. The first piezoelectric nanogenerator (PENG) was developed in 2006 by Wang *et al*. It had an efficiency of 17-30%. They synthesized their NG by using ZnO NW grown on an aluminum oxide Substrate [2]. Later, in 2009 a new design of ZnO PENG was developed by growing ZnO NWs on a flexible substrate [3]. Following that, and up to this day, research dedicated to increasing the efficiency of NGs has been at its peak due to the huge advantages that can be achieved with this technology. Various attempts were made by using different substrate materials and stacking PENG layers on top of each other [4]. Fig.1 below shows a brief history of PENG research development.
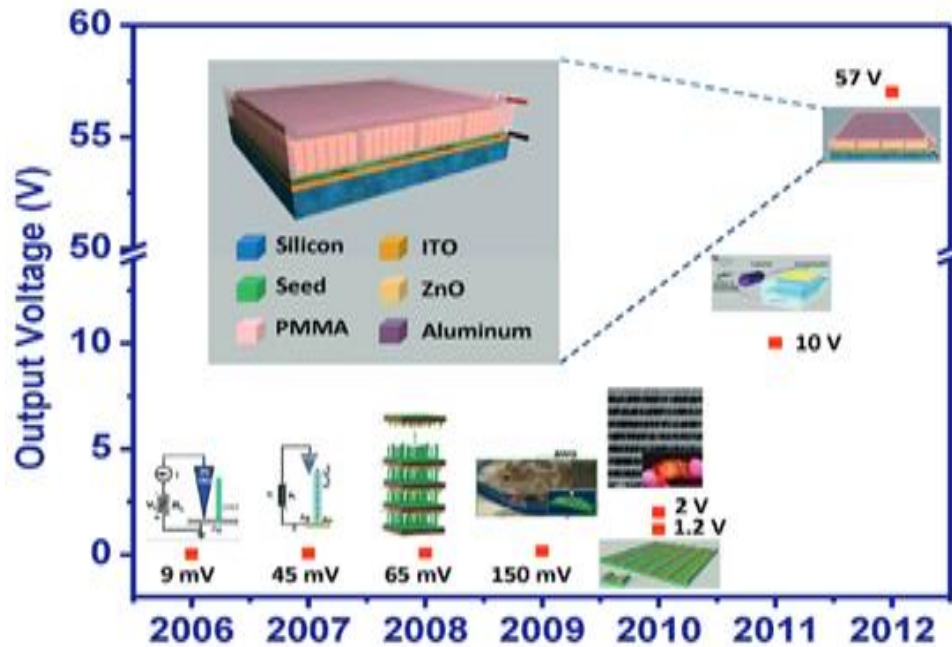
Figure 1: A brief history of PENG research development (adapted from: [4]).

NGs' main advantage is their ability to harvest wasted energy (mechanical or thermal) and turn it into electricity. It has broad applications such as powering biomedical devices, nano-sensors, and nanodevices. It also has simply provided means to benefit from the abundant sources of energy around us. Imagine the ability to turn body movements, muscle contraction, traffic movements, wind, and many other mechanical and thermal sources into electricity.

In this thesis, the main focus will be on PENGs. The following tasks will be covered in detail:

- Synthesis of ZnO NWs with the aim of high Aspect Ratio (AR).
- Defect characterization of ZnO NWs via spectroscopic techniques such as electron paramagnetic resonance (EPR) spectroscopy, photoluminescence (PL) spectroscopy, X-ray diffraction (XRD), and scanning electron microscopy (SEM).
- Exploring methods to introduce defects into ZnO structure by doping ZnO with transitional metal ions (TMI) or ball milling to reduce ZnO particles size into the nanoscale.
- Exploring methods to maximize the piezoelectric coefficient d_{33}.

2. State of art

2.1.   Types of NGs

NGs can be divided into three main types based on their working mechanism and the physical property of the materials system, namely:

- Triboelectric NG.
- Pyroelectric NG.
- Piezoelectric NG.

Triboelectric NG converts the energy due to contact between two surfaces into electrical charge. The electrical charge generated depends on many factors such as the nature of the two surfaces, the amount of rubbing between the surfaces, and the surface area [5]. The principle is straightforward, and the triboelectric effect has been noticed since ancient times (the effect of rubbing amber with a piece of clothes gave it the ability to attract light objects such as pieces of paper).

Pyroelectric NG (as the name suggests) are devices that can convert thermal energy into electrical energy. It depends on the pyroelectric effect which occurs when certain materials develop a polarization change due to temperature changes. It can be extremely useful and beneficial to convert thermal energy into electricity because according to professor Zhong Lin, more than 50% of the energy generated in the United States is lost in the form of heat [6].

PENGs are devices that convert mechanical stress into electrical charge. The fact that PENGs do not depend on external conditions such as temperature makes them unique, also the reversibility of the process even makes them more special, and increases the applications of PENGs. PENGs can be used to harvest energy from wide sources such as body movements, traffic, air conditioning airflow, and many other sources. The harvested energy can be used to power microdevices [2, 7, 8]. Many researchers are aiming to increase the efficiency of PENGs to increase the benefits of this technology, especially since mechanical energy sources are abundant and easy to access [9].

2.2.   The piezoelectric effect

The piezoelectric effect was first discovered by the two Curie siblings, Pierre and Jacques in 1880. They were experimenting with applying pressure on quartz crystal, which led to a release of an electrical charge, and they called it the piezoelectric effect [10]. When a piezoelectric material experiences mechanical stress, the perfectly balanced crystals are disturbed by this change, and the balance is broken which in return forces electric charges out of balance. By placing piezoelectric material in between two metallic plates, this charge can be used to create a voltage, and an electrical circuit can be created, as shown in Fig.2 below.
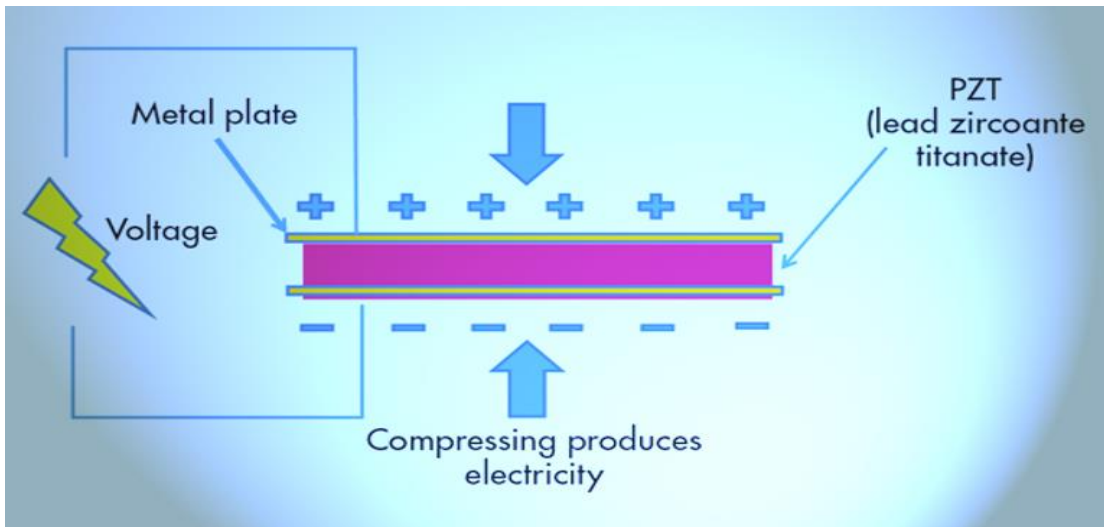
Figure 2: Working principle of direct piezoelectric effect (adapted from: [11]).

This process is reversible, the opposite can happen when an electrical charge is applied to the piezoelectric material. The voltage causes the crystals to either shrink or expand, which causes the release of sound waves from the crystals as shown in Fig.3 below.
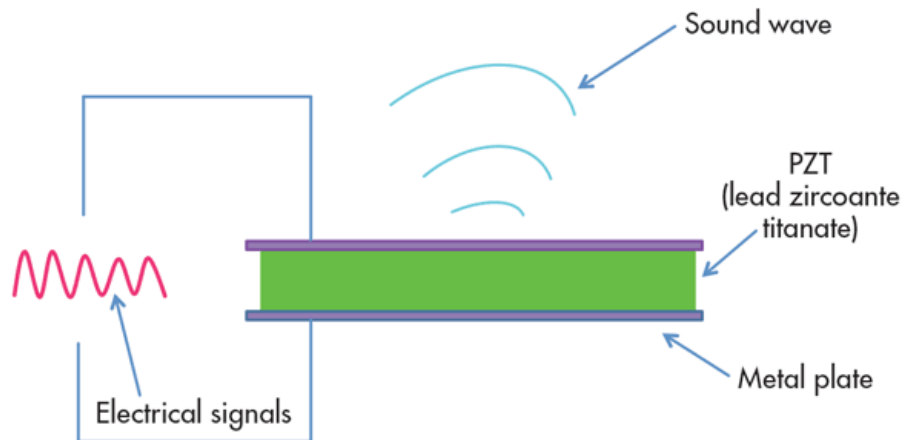
Figure 3: Working principle of reverse piezoelectric effect (adapted from: [11]).

As mentioned before, PENGs are unique due to their independence from external conditions such as temperature and humidity. The reversibility of the piezoelectric effect also tremendously increases the applications of piezoelectric materials. Below are some examples of the applications of piezoelectric materials:

- Gas sensors: electrical conductivity of piezoelectric materials is affected when gas molecules interact with their surface.
- Bio-sensors: bio-safe piezoelectric materials such as ZnO can be used for a wide range of biomolecular interactions.
- Voice recognition systems: widely used in mobile phones and security systems. Specific voice patterns can trigger different commands.

The following classification can be made for piezoelectric materials:

- Naturally occurring crystals: quartz, Rochelle salt, topaz ($Al_2SiO_4F_2$).
- Ceramics: ZnO, lead zirconium titanate (PZT), barium titanate ($BaTiO_3$).
- Biological molecules: silk, tendon, collagen.
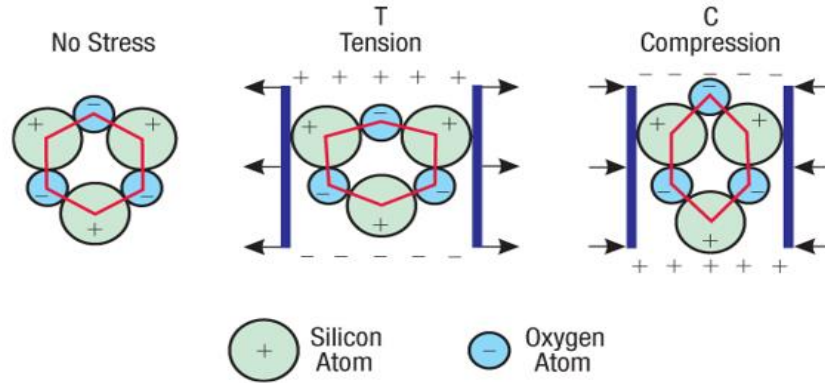
Figure 4: Piezoelectric effect in quartz crystal (adapted from: [11]).

As can be seen from Fig.4 above, when a quartz crystal is relaxed (not under any stresses), the electric charge distribution inside the crystal lattice is balanced even though the crystal is asymmetric. However, once it experiences stress, a quartz crystal produces electricity due to the creation of a polarity inside the crystal structure as a result of disturbing the electric neutrality inside the crystal structure. This property is only observed in asymmetrical crystal structures.

The most important parameter of piezoelectric materials is the piezoelectric coefficient d_{33}. In general, materials with a higher piezoelectric coefficient yield a higher piezoelectric effect [7, 12, 13].

$$P = d \cdot S \qquad (1)$$

P: polarization.
d: piezoelectric coefficient.
S: strain.

This is the simplified relation for the piezoelectric coefficient between polarization and applied stress. However, the actual calculation of this coefficient is much more complicated, and it also involves calculating the efficiency of the generated electricity when stress is applied, and on the other hand, the amount and direction of mechanical deformation (strain) when piezoelectric materials are subjected to electricity (reverse piezoelectric effect) [14].

The selection of convenient piezoelectric material depends mainly on the application and the piezoelectric coefficient.

Two main materials that are mostly used as piezoelectric nanogenerators are PZT and ZnO NW. Although PZT provides a higher value for piezoelectric coefficients d_{33} and d_{32}, where d_{XY}: (d) Indicates piezoelectric coefficient -(X) Indicates the direction of polarization, (Y) indicates the direction of mechanical stress- ZnO is used more frequently due to safety considerations caused by the presence of lead in PZT. In addition to that, ZnO exhibits both piezoelectric and semiconductor properties which makes it an ideal option for many applications [15].

Table 1 shows the differences in calculated values of some piezoelectric materials adapted from various studies [16-18].

Table 1: Piezoelectric coefficient d33 of different materials (adapted from: [2, 17, 18]).

Material	Structure	Piezoelectric coefficient d_{33} (pC/N)
ZnO	Nanowire	10 - 15
PZT	Nanowire	90
$NaNbO_3$	Nanowire	1 - 4.26
$BaTiO_3$	Nanowire	0.5

Piezoelectric coefficient d_{33} can be significantly increased by increasing the aspect ratio of the NWs. Increasing the length of the NWs, and decreasing their diameter causes easier stressing, thus increasing the polarization and enhancing the piezoelectric effect [19].

As can be seen from Table 1 above, ZnO exhibits a good piezoelectric coefficient d_{33} compared to other materials such as $NaNbO_3$ and $BaTiO_3$. Though it is not as high as PZT, being bio-safe, and non-toxic makes ZnO a better candidate for many applications. In the next section, the properties of ZnO will be discussed.

2.3.   Properties of ZnO:

ZnO is classified as a semiconductor metal oxide with a wide and direct bandgap energy of about 3.3 eV. ZnO can crystallize in a hexagonal wurtzite structure or a cubic zinc blend. Under normal conditions, ZnO exhibits a hexagonal wurtzite structure as shown in Fig.5 below [9].
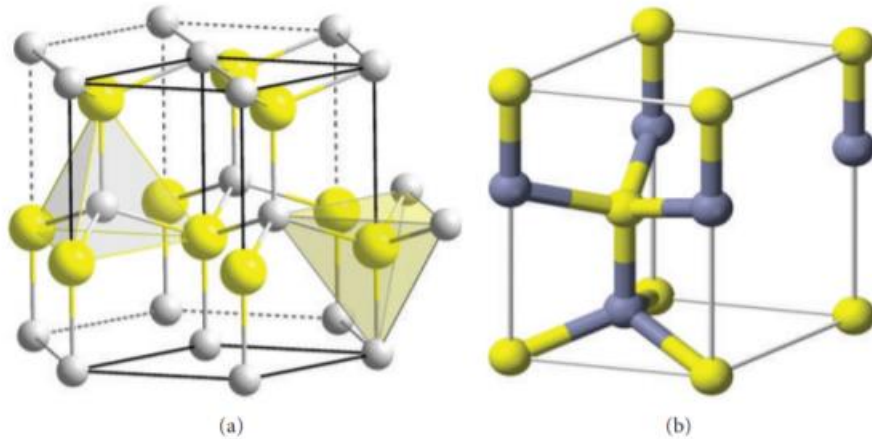
Figure 5: ZnO crystal structure (yellow Zn – grey O) (a) hexagonal wurtzite structure (b) hexagonal wurtzite unit cell (adopted from [9]).

Under the influence of high pressure, ZnO exhibits a cubic crystal structure with an indirect bandgap of around 2.7 eV [20]. Table 2 below summarizes some of the physical properties of ZnO [9, 20, 21].

Table 2: Physical properties of ZnO.

Property	Value
Crystal structure	Hexagonal wurtzite at 300 °K
Lattice constants a,b,c	a= 0.32495 nm b= 0.32495 nm c= 0.52069 nm
Melting point	1975 °C
Density	5.66 g/cm^3
Bandgap energy E_g	3.3 eV (direct energy gap)
The effective mass of electrons	0.24
The effective mass of holes	0.59
Refractive index	2.01
Exciton binding energy	60 meV
Dielectric constant	8.656

As can be seen from Table 2 above, the ratio of lattice constants $\frac{c}{a} = 1.6333$ which corresponds to the ideal ratio of wurtzite structure 1.6. ZnO exhibits a high exciton binding energy of 60 meV, which makes it an ideal candidate for many optical devices [22, 23]. The optical properties of ZnO can be understood by studying its intrinsic and extrinsic features. Intrinsic features are directly linked to the interaction between holes in the valence band VB, and electrons in the conduction band CB. While extrinsic features are linked to doping, or in other words, introducing defects in the structure of ZnO. These defects can be one or more of the following:

- Oxygen vacancy (V_O).
- Oxygen interstitial (O_i).
- Zinc vacancy (V_{Zn}).
- Zinc interstitial (Zn_i).

A clear understanding of the effect of these defects will be displayed in the results section of EPR and PL analysis, and there has been a considerable amount of research dedicated to understanding the defect structure of ZnO [24-27]. It is also worth mentioning that ZnO is an n-type semiconductor naturally, but it can be converted into p-type semiconductor by introducing intrinsic or extrinsic defects into its structure by the aforementioned techniques [28, 29].

As for the magnetic properties of ZnO, it is a paramagnetic semiconductor in normal circumstances. However, by doping it with Transition Metal Ion (TMI), it can become a Dilute Magnetic Semiconductor (DMS) material. TMI such as Mn, Fe, Cr, Co, Cu, and others alters the electronic configuration of ZnO. These doping elements have moderately filled d and f orbitals, and one orbital is incompletely filled (having down or up spins). For example, Mn^{+4} replaces Zn^{+2} in the ZnO structure, and imparts $4s^2$ electrons into sp^3 orbitals, ultimately creating a DMS material. DMS materials are used in spintronic devices and have a great potential for research applications [25, 30, 31].
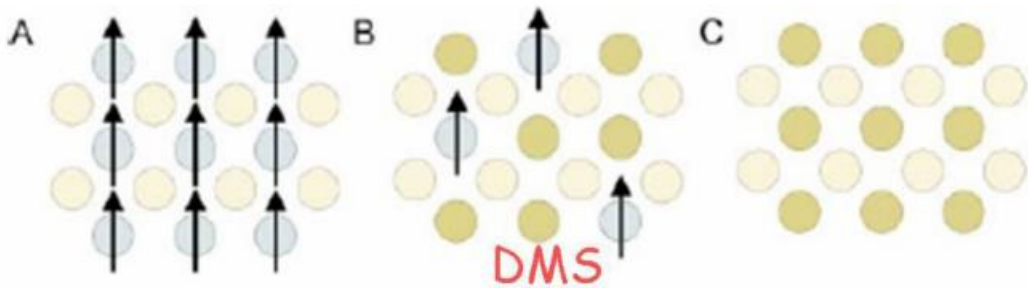
Figure 6: (A) Magnetic semiconductor (B) DMS (C) Nonmagnetic semiconductor (adapted from: [20]).

3. Materials and synthesis:

In this section, we will mainly focus on ZnO NWs synthesis. NWs, also known as 1D (when the wires length in micro-scale, and diameter in nanoscale) hold significant importance because electrons' moments are confined in two directions, thus the electrons can move in only one direction [32], as can be seen in Fig.7.
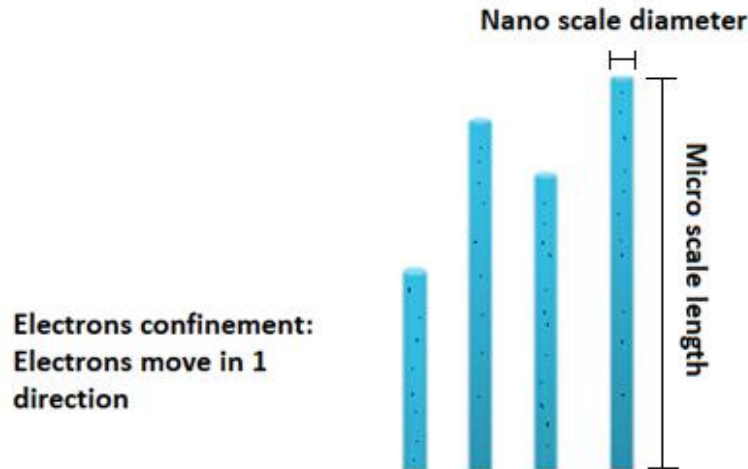
Figure 7: Electrons confinement and movement in 1 direction due to NWs morphology.

ZnO NWs can be synthesized by using a wide range of methods, each of which has its advantages and is recommended for a particular application:

- Vapor Phase Synthesis: It is classified into Vapor Liquid Solid (VLS) and Vapor Solid (VS) growth. As the name suggests, this method utilizes gaseous precursor reactants to synthesize NWs. Having the reactants in the gaseous phase yields an easy manipulation of the nanostructure of crystals, and in turn, it produces crystalline and defect-free NWs [32].

- Physical Vapor Deposition (PVD): Uses either Radio Frequency (RF) sputtering or thermal evaporation to synthesize NWs. In its evaporated form, ZnO is directly deposited on substrates to form the required NWs. On the other hand, solid ZnO is used in R.F sputtering. Required growth of NWs can be controlled by temperature, champer pressure, and gas flow rate [9].

- Chemical Vapor Deposition (CVD): Used to produce NWs at large scales and low temperatures compared to VLS. CVD uses ZnO sources to chemically deposit ZnO on substrates (such as silicon). The main advantages of this method are the relatively low temperatures and the high purity ZnO NWs [32].

- Solution Phase Synthesis (also known as hydrothermal synthesis): ZnO NWs are synthesized by using an aqueous solution [9, 32, 33]. The precursor materials are dissolved in a solution, and the reaction occurs endothermically, to finally produce ZnO NWs. In this study, the main focus will be on the hydrothermal method. Owing to its simplicity, low cost, and low-temperature synthesis. To be more precise, the main focus will be on the developed microwave-assisted hydrothermal method, which uses a conventional microwave oven as a source of heat for the reaction, instead of heat.

3.1. ZnO microwave-assisted hydrothermal synthesis:

Similar to the classic hydrothermal approach, the microwave-assisted approach also involves dissolving the precursor materials in a solution, usually DI water The main difference is in the supplied energy for the reaction. The microwave-assisted method as the name suggests provides the required energy for the reaction in the form of microwaves by using a conventional microwave oven.

The main advantages of using the microwave-assisted method over the classical hydrothermal method can be listed as follows:

- More facile, and the apparatus is rather simple.
- Way much faster, as it only takes about 15-20 minutes of heating in the microwave, while it takes about 8 hours in the heating oven.
- Easier control of temperature, as the temperature in the microwave, is constant (about 90° C regardless of microwave power output), and the only control parameters are microwave power output and time.
- The reaction occurs at atm pressure, and there is no need to use a hydrothermal autoclave, thus pressure control is eliminated from the process.
- Better distribution of energy and less energy loss since the process is contact-less.

Table 3 below shows the precursor material for pure and Mn-doped ZnO NWs synthesis.

Table 3: Chemicals that have been used for synthesizing pure and Mn-doped ZnO NWs.

Precursor	Chemical Formula	Cas No.	Manufacturer	Molecular Weight (g/mol)	Density (g/cm^3)
Zinc Nitrate Hexahydrate	$Zn(NO_3)_2.6H_2O$	10196-18-6	Acros Organics	297.48	2.065
Hexamethylenetetramine	$C_6H_{12}N_4$	100-97-0	Merck	140.19	1.331
Manganese Acetate Tetrahydrate	$C_4H_6MnO_4$	6156-78-1	Acros Organics	245.09	1.589
Methanol (pure) for analysis	CH_3OH	67-56-1	Sigma Aldrich	32.04	0.792

Factors affecting the hydrothermal growth of ZnO NWs:

- Effect of using HMTA: lots of studies were conducted on the effect of using HMTA as a precursor for ZnO NWs hydrothermal growth, and the results were controversial. HMTA is a highly water-soluble nonionic heterocyclic amine [34]. HMTA works as a pH buffer and is the main source of OH⁻ ions [35]. The following reactions occur as a result of hydrothermal synthesis of ZnO NWs:

$$(CH_2)_6N_4 + 6H_2O \rightarrow 6HCHO + 4NH_3 \qquad (2)$$

$$NH_3 + H_2O \longleftrightarrow NH_4^+ + HO^- \qquad (3)$$

$$Zn(NO_3)_2 \rightarrow Zn^{+2} + 2NO_3^- \qquad (4)$$

$$Zn^{+2} + 2HO^- \longleftrightarrow ZnO + H_2O \qquad (5)$$
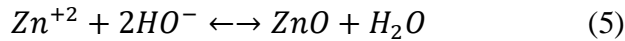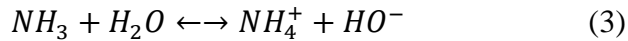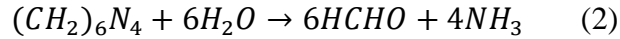
HMTA hydrolyses as a result of providing it with energy from the microwave, which forms formaldehyde and ammonia as shown in equation 2. After that, ammonia reacts with water to produce OH⁻ ions as shown in equation 3. Zinc nitrate forms Zn^{+2} ions as shown in equation 4. Finally, a direct crystallization process occurs as shown in equation 5, and the final product is ZnO NWs.

Another indirect crystallization process can occur as follows:

$$Zn^{+2} + 2HO^- \longleftrightarrow Zn(OH)_2 \qquad (6)$$

$$Zn(OH)_2 \longleftrightarrow ZnO + H_2O \qquad (7)$$
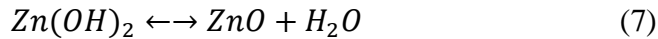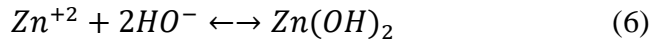
The reactions shown in equations 6 and 7 cause the formation of hydroxide impurities [36], as will be shown later in the XRD results section.

- Effect of precursors on AR: Using low molar concentrations of HMTA and Zinc Nitrate Hexahydrate ZNH causes the increase in AR as per previous reports [19, 37]. Additionally, by following the microwave-assisted hydrothermal route, it is rather easy to control the AR of the NWs simply by adjusting the microwave power output [25] as will be shown in the SEM results section. Microwave-assisted hydrothermal synthesis allows homogenous distribution of energy throughout the precursor solution, which in turn leads to homogenous crystallization as shown in Fig.8. This yields higher quality NWs with higher AR, thus a higher piezoelectric effect [38].
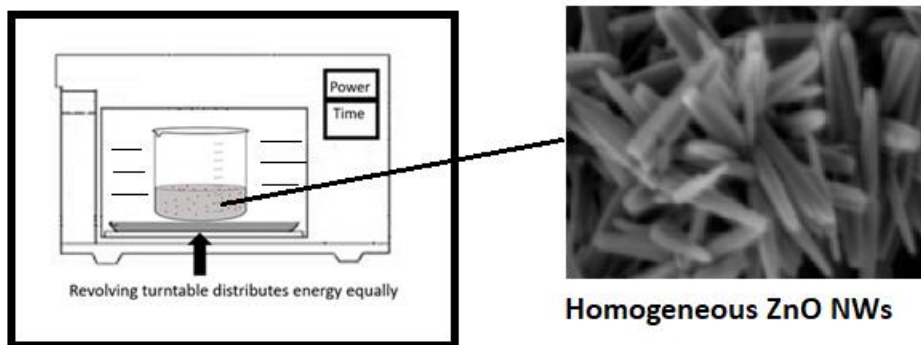
Figure 8: Homogenous growth of ZnO NWs by the microwave-assisted method.

3.2. Experimental:

For the synthesis of pure and Mn-doped ZnO NWs, an original synthesis route has been followed that was developed by Tian et al. [25, 39]. Additionally, a microwave oven has been used as a source of energy for the reaction instead of a conventional oven as in the original synthesis route. An equimolar solution of 25 mM ZNH and HMTA is dissolved in deionized (DI) water and magnetically stirred for 1 h at 500 RPM. The solution is then heated in a commercial microwave oven for 20 minutes, by using different microwave power outputs (160 W, 320 W, and 800 W). After leaving the microwave, ZnO NWs are separated from the solution by using filtering papers. Lastly, ZnO NWs powder is dried in the oven at 80° C for 9 hours. The same process is used for synthesizing Mn-doped ZnO NWs, but by mixing ZNH and HMTA solution with Manganese Acetate Tetrahydrate (MAT) dissolved in 50 mL methanol. Amounts of MAT are chosen according to desired dopant mol% (2 mol%, 5 mol%, and 10 mol%). The process is illustrated in Fig.9 below.

(i) ZNH and HMTA are dissolved in DI water.

$Zn(NO_3)_2.6H_2O + C_6H_{12}N_4$

DI Water

(ii) MAT is dissolved in 50 ml methanol.

$C_4H_6MnO_4$

50 ml Methanol

(i) and (ii) are mixed together and the mixed solution of 25 mM is magnetically stirred at room temperature for 1 hour at 500 rpm

25 mM $Zn(NO_3)_2.6H_2O$ + $C_6H_{12}N_4+C_4H_6MnO_4$

Magnetically stirred at 500 rpm for 1 h
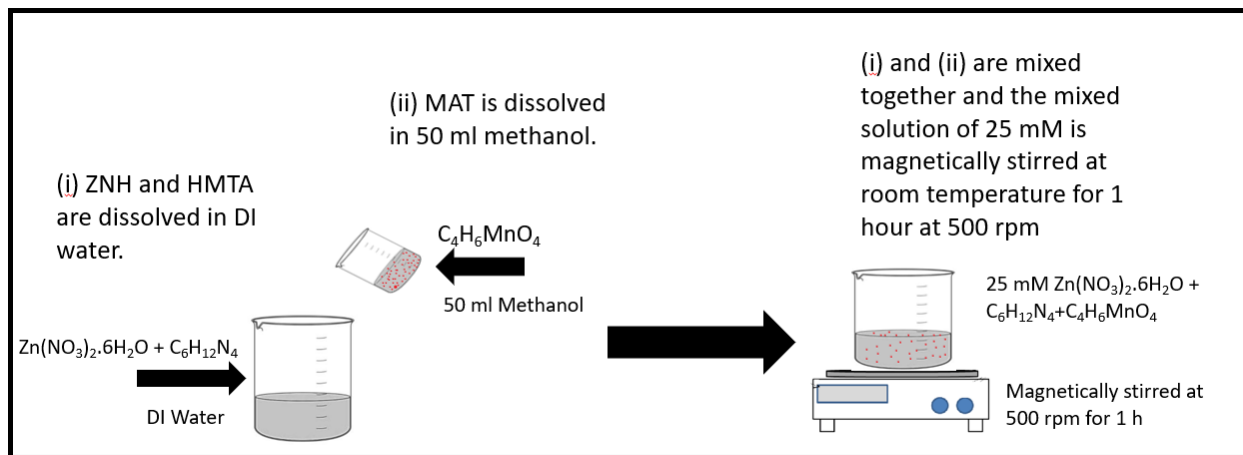
Figure 9: Schematic representation of the microwave-assisted hydrothermal synthesis of pure and Mn-doped ZnO NWs.

Main Control parameters of microwave-assisted hydrothermal synthesis process:

- Microwave power: Using higher microwave power output favors nucleation [40]. Thus, it yields more dense NWs, and the doping process is more effective. However, the synthesized NWs will suffer from less AR than using lower microwave power.

- Dopant concentration: Introducing extrinsic defect structure into ZnO NWs can be achieved by doping it with Mn ions. Both Zn and Mn ions have the same oxidation number of +2, and their ionic radius is similar (0.68 Å) and (0.75 Å) respectively. Thus, Mn^{+2} ions replace Zn^{+2} ions in the structure, which introduces DMS properties [41]. ZnO NWs with varying Mn dopant concentrations are synthesized and studied in the results section.

- Heat treatment: To ensure an effective doping process where Mn^{+2} ions are fully incorporated into the structure of ZnO NWs, some heat treatment is required for the microwave-assisted synthesized samples. Heat treatment temperature and time are optimized and displayed in EPR results section.

4. Methods:

4.1. XRD analysis:

The crystal structure of the ZnO NWs was tested by X-Ray Diffraction (XRD) performed using Bruker D2 Phaser diffractometer. The diffractometer uses Cu Kα X-ray with a wavelength λ = 0.154 nm in the 2θ range from 25° to 85°. The XRD results were also used to calculate the average crystalline size using both the Scherrer equation and Williamson-Hall plots.

4.2. SEM analysis:

The microstructure morphology of the ZnO NWs was tested by Scanning Electron Microscope (SEM) performed using JEOL JIB-4501 Multibeam FIB/SEM System). SEM was operated at 5 kV. SEM images were used to calculate the average NWs length, diameter, and AR.

4.3. EPR spectroscopy:

Electron Paramagnetic Resonance (EPR) measurements were carried out using Bruker EMX Nano with an integrated referencing for g-factor, the microwave frequency used was 9.63 GHz (X-band) and all measurements were done at room temperature with 2 G modulation amplitude, 10 mW microwave power with 50 scans. Applying an external magnetic field with Zeeman splitting, the resonance condition is fulfilled:

$$g_e = \frac{h\nu}{\beta_e B_0} \qquad (8)$$

h: Planck's constant.

v: Frequency of electromagnetic radiation.

β_e: Bohr magneton.

B_0: Magnetic field.

g_e: Electron's g factor with value of 2.0023 for free electrons, which holds special importance in EPR spectroscopy as each material has its fingerprint g factor. Studying EPR spectra helps in understanding the defect structure of ZnO NWs, and to determine the effectiveness of the doping process.

4.4. PL spectroscopy:

The optical properties of the ZnO NWs were tested by Photoluminescence (PL) using Edinburgh Instrument Spectrofluorometer FS5. The samples were tested at room temperature with an excitation of 320-370 nm (varies from sample to sample) and slit distance for excitation and emission of 5 and 10 nm, respectively.

4.5. High Energy Ball Milling (HEBM) processing:

HEBM was performed to introduce intrinsic defects into the ZnO NWs structure. HEBM was performed at room temperature using the Fritsch^{TM} Pulverisette planetary milling machine Premium Line 7 with two grinding stations of 45 ml volume each. 10 mm balls of zirconium oxide (ZrO_2) were used for grinding, and the balls-to-powder ratio was adjusted for all samples to 10:3.

4.6. Piezoelectric coefficient d_{33} measurement:

The piezoelectric coefficient d_{33} measurements were performed by D33PZO1 piezometer from Marine India. The system was operated at 252 N static force and 0.25 N 110HZ amplitude dynamic force.

5. Results and Discussion:

5.1. XRD Analysis:

The crystal structure of all samples was investigated by performing XRD tests on the synthesized samples. XRD results show the phases of the crystal structure and can be also used to calculate the average crystallite size. Fig.10 below shows the XRD plots of ZnO NWs produced by the microwave-assisted hydrothermal method.
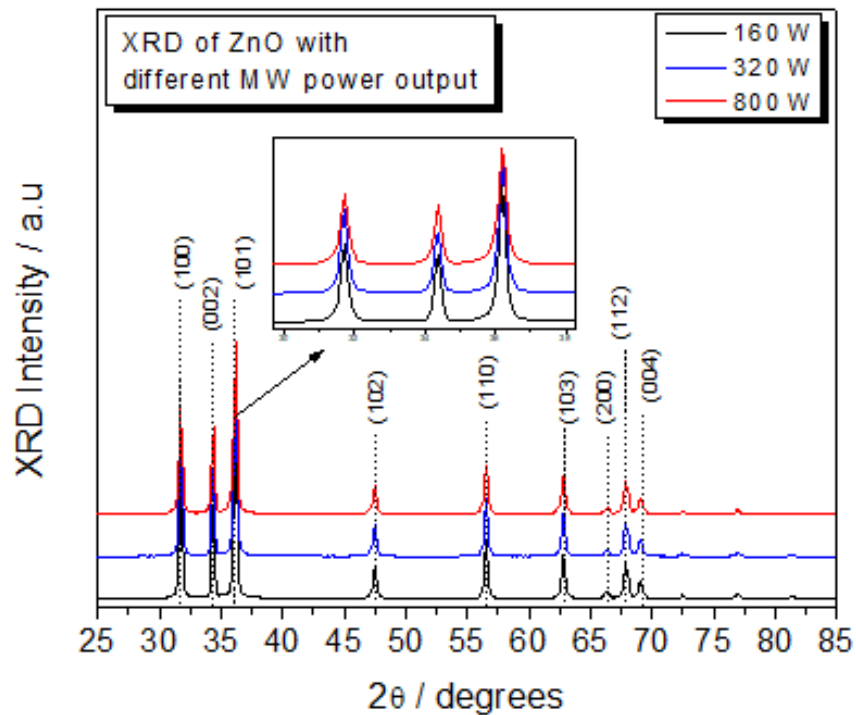
Figure 10: XRD plots of pure ZnO NWs produced with different microwave power outputs.

It can be noticed that all 3 samples show the typical wurtzite structure peaks of ZnO with peaks of miller indices at (100), (002), (101), (102), (110), (103), (200), (112), (004).

Scherrer equation was used to evaluate the average crystallite size:

$$D = \frac{K\lambda}{\beta_D \, Cos\theta} \qquad (9)$$

Where D: average crystallite size in nm.

K: shape factor that depends on the lattice shape.

λ: wavelength of X-ray source (0.154 nm).

β_D: broadening of peaks due to crystals size (radians).

θ: peaks angle (radians).

It is worth mentioning that the Scherrer equation only considers the broadening of the peaks due to crystals size, and doesn't consider the broadening due to strain. In addition to that, it is only valid for the nanoscale. To add broadening due to the strain effect, Williamson Hall (W-H) plots method is used [42].

$$\beta_t = \beta_D + \beta_\varepsilon \qquad (10)$$

Where β_t: total broadening (radians).

$\beta_D = \frac{K\lambda}{DCos\theta}$: broadening due to crystals' size (radians).

$\beta_\varepsilon = 4\varepsilon Tan\theta$: broadening due to strain (radians).

By re-arranging, we obtain:

$$\beta_t Cos\theta = \frac{K\lambda}{D} + 4\varepsilon Sin\theta \qquad (11)$$

Which takes the form of a linear equation. W-H plots are used to obtain the average crystallite size D and the strain ε from the y-intercept, and the slope of the linear equation.

Table 4 below shows the results of average crystallite size obtained from the Scherrer equation and W-H plots, and Fig.11 shows the W-H plots fitted lines.

Table 4: Average crystallite size calculations of pure ZnO samples, by the Scherrer equation and W-H Plots.

Sample's microwave power output (W)	Scherrer equation average D (nm)	W-H plots average D (nm)
160	26.5	62.5
320	26.5	62.5
800	26.5	60
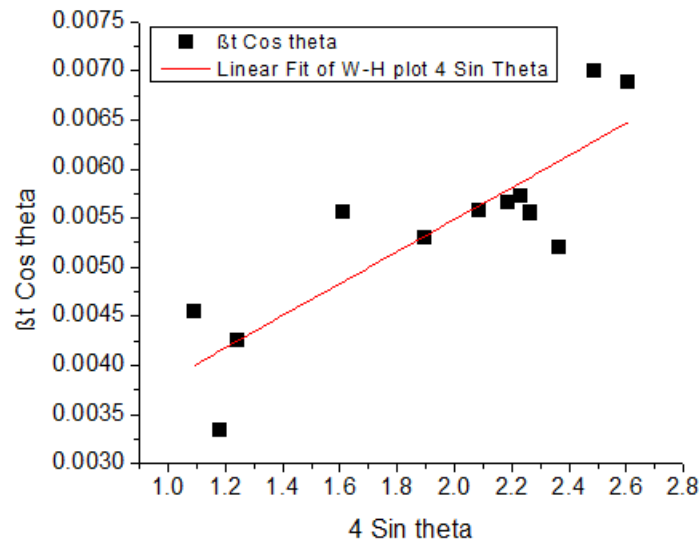
Figure 11: W-H Plots linear fitted line.

A similar average crystallite size can be noticed for all the calculations from both Scherrer's equation and W-H plots for all 3 samples, mainly due to similar crystalline structures. It is worth mentioning that the average crystallite size differs from the actual particles size. Under no circumstances shall the average particles size be higher than the average crystallite size since particles might be composed of several single crystals. An analysis of average particles size will be demonstrated in SEM results section.

Fig.12 below shows the XRD plots of Mn-doped ZnO NWs with different Mn concentrations, synthesized by a microwave-assisted method at 800 W microwave power output.
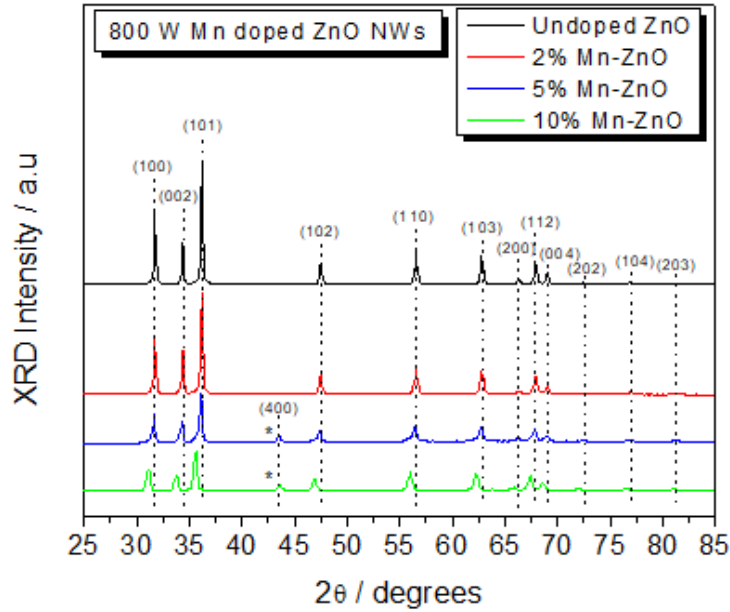
Figure 12: XRD plots for Mn-doped ZnO samples with varying Mn concentrations synthesized with 800 W microwave power.

It can be observed that all samples show the typical wurtzite structure of ZnO, which means that Mn doping does not alter the crystalline structure of ZnO. However, Mn doping causes a slight shift towards smaller 2θ values, due to the small difference between the ionic radii.

Scherrer equation and W-H plots were applied to calculate the average crystallite structure as shown in table 5 below.

Table 5: Average crystallite size calculations of Mn-doped ZnO samples, by the Scherrer equation and W-H Plots.

Mn Concentration (%)	Scherrer equation average D (nm)	W-H plots average D (nm)
0	26.5 ±2	60.0 ±2
2	27.0 ±2	56.6 ±2
5	24.8 ±2	36.0 ±2
10	19.8 ±2	24.0 ±2

Increasing Mn mol% leads to a decrease in average crystallite size as can be shown in table 5. These results were expected and explained in various studies of Mn-doped ZnO [43, 44].

Finally, the formation of an additional peak can be observed (marked with * in the graph) at around $2\theta° = 43.5°$ (400) for 5%Mn-ZnO and 10%Mn-ZnO samples corresponding to $ZnMnO_3$ impurity which forms as an additional phase in the structure as a result of decomposition due to increased exposure to heating energy [43, 45].

Fig.13 below shows the XRD plot for bulk ZnO purchased from sigma Aldrich and ball-milled samples of the same ZnO as a function of milling time.
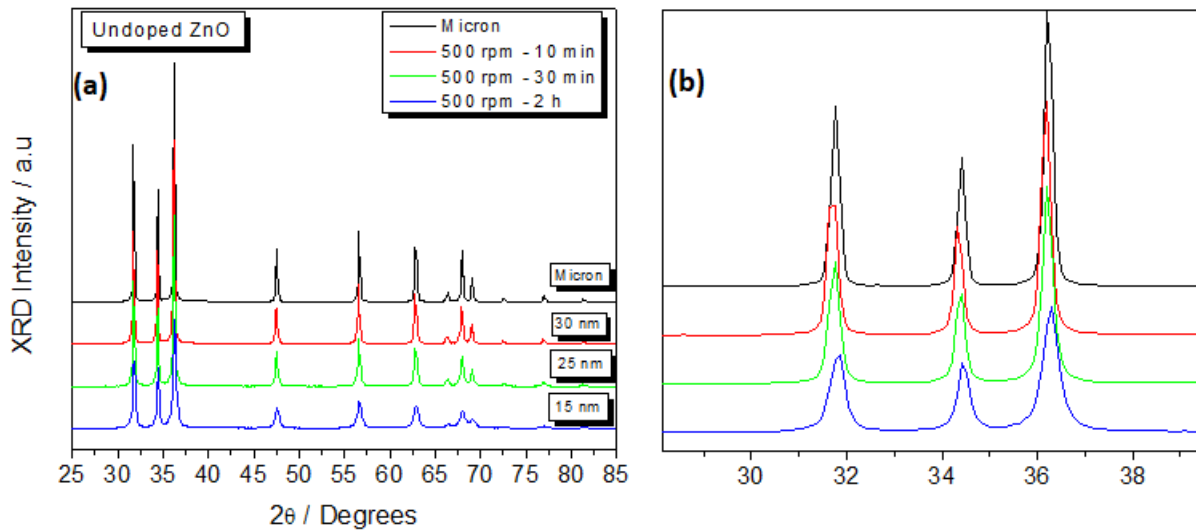
Figure 13: (a) XRD plot for pure ZnO samples with varying milling times (b) peak broadening of the main 3 peaks.

The effect of ball milling can be observed from the broadening of the peaks. It can be noticed that increasing the milling time causes the major peaks to broaden, which in turn indicates a smaller average crystallite size.

Table 6 and Fig. 14 below show the calculated average crystallite size as a function of time.

Table 6: Average crystallite size calculations for ball-milled ZnO samples as a function of milling time.

Milling time at 500 rpm	Scherrer equation average D/nm	W-H plots average D/nm
Unmilled	Bulk	N/A[*]
10 min	30	76
30 min	25	73
2 h	15	N/A[**]

[*]: Not applicable because the samples are not in the nano-scale.
[**]: Not applicable because the obtained y-intercept was negative.
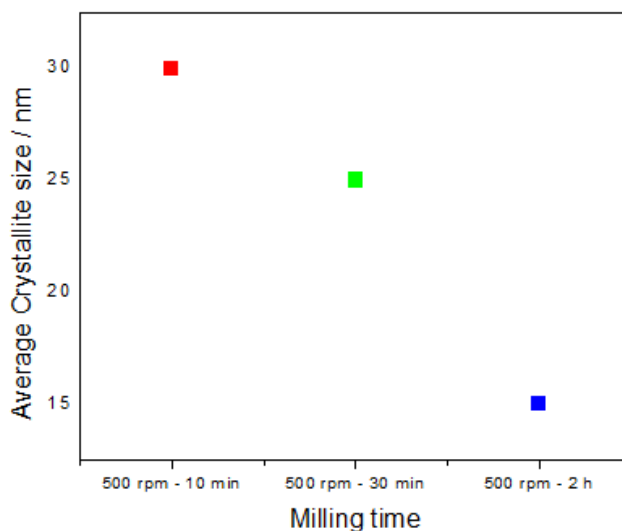
Figure 14: Effect of ball-milling time on average crystallite size.

As can be observed from table 6 above, it is not applicable to use Scherrer's equation and W-H plots on bulk samples since they are not in the nano-scale. In addition to that, 2 hours of ball-milled samples yielded a negative y-intercept in W-H plots, which indicates that the broadening due to strain is not relevant in this case.

The results of ball-milling time will be explained more thoroughly in EPR and PL sections.

5.2. SEM Analysis:

The morphology and average particles size distribution of the synthesized samples were tested by studying the SEM images of the samples.

Fig.15 below shows the SEM images of pure ZnO samples synthesized at 160 W, 320 W, and 800 W from left to right respectively. Below the SEM images, the histograms of average wire diameter and average wire length are included, as per analyzed by using ImageJ software. Table 7 below summarizes AR calculations for the samples.
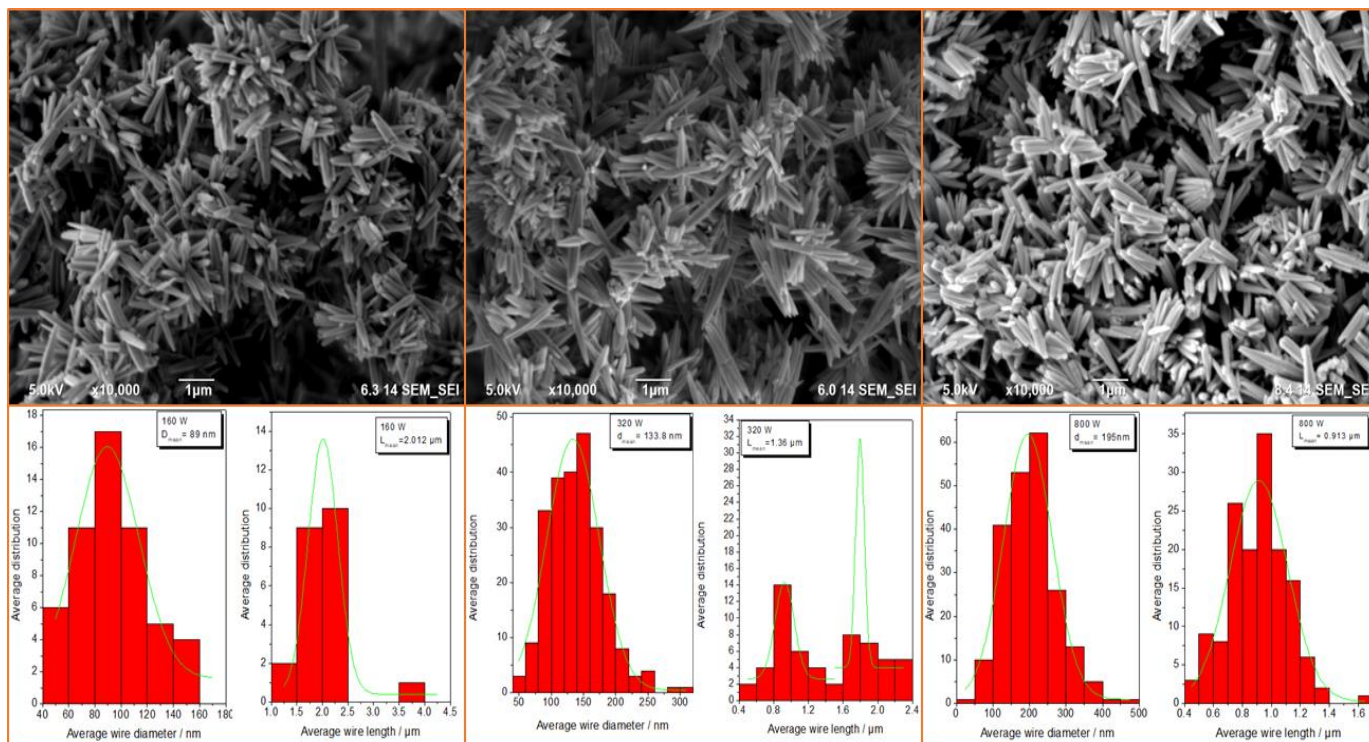
Figure 15: SEM images and histograms of average wire diameter and length for ZnO samples with microwave power outputs of 160 W, 380 W, and 800 W from left to right.

Table 7: AR calculations for pure ZnO samples with a varying microwave power output.

Microwave power/ W	Average wire diameter/ nm	Average wire length/ μm	AR
160	89	2.012	22.6
320	134	1.36	10.1
800	195	0.913	4.7

As can be seen from Fig.15 above, all samples exhibit the NWs – nanorods morphology. As per the reported studies, higher microwave power output favors nucleation, and it yields NWs with

higher densities than samples with lower microwave power. However, samples with lower microwave power yield a higher aspect ratio as can be concluded from table 7 above.

Fig.16 below shows the SEM image of 5%Mn-ZnO synthesized by microwave-assisted hydrothermal method with 800 W microwave power, with histograms of average wires diameter and length below the image. Table 8 summarizes AR calculations of Mn-doped ZnO samples.
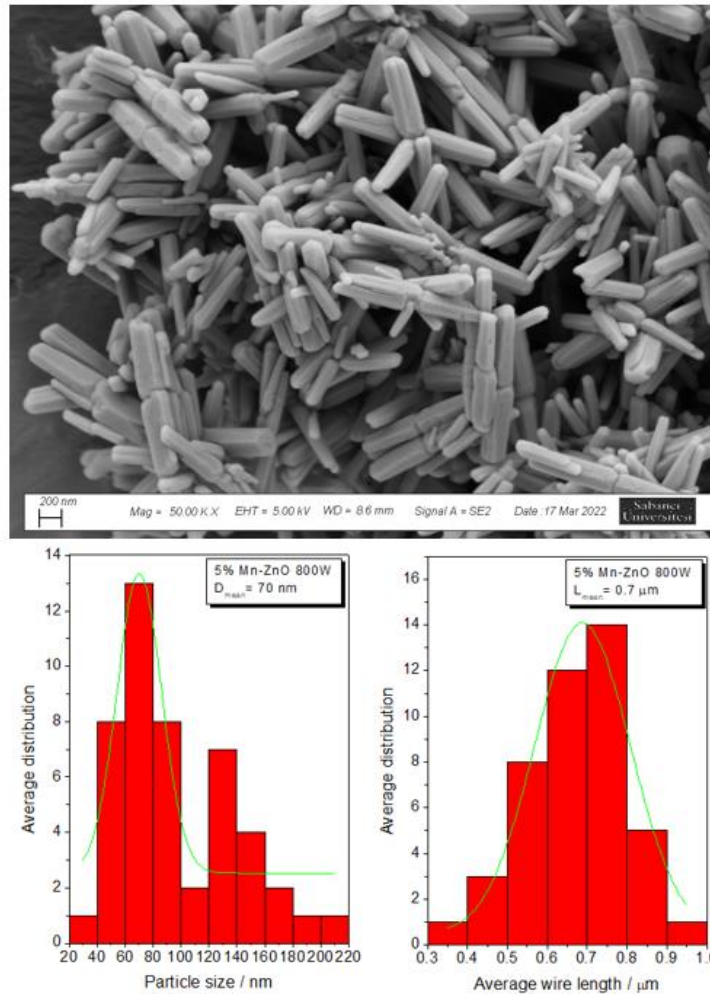
Figure 16: SEM image of 5%Mn-ZnO synthesized by microwave-assisted hydrothermal method, histograms of average wires diameter and length below the image.

Table 8: AR calculations of 5%Mn-ZnO sample.

Microwave power/ W	Average wire diameter/ nm	Average wire length/ μm	AR
800	70	0.7	10

As can be seen from Table 8 above, the calculations are in good agreement with Scherrer's equation calculations. It can be observed that Mn-doping leads to a decrease in the particles size. In addition to that, we can observe a decrease in average wires length as well, but the AR is higher than undoped samples synthesized with 800 W microwave power.

By comparing the wires morphology of undoped and Mn-doped samples, we notice a slight difference in the tip of the wires. Undoped samples seem to have a pointy tip, Mn-doped samples on the other hand seem to have a blunt tip as can be seen in Fig.17 below.
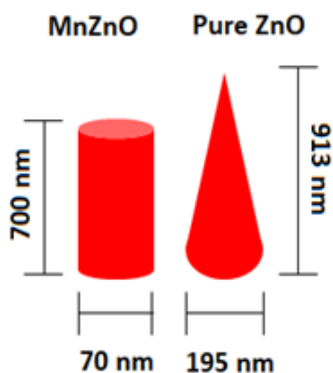
Figure 17: Comparison between Pure and Mn-doped ZnO nanowires.

5.3.EPR Analysis:

EPR spectroscopy plays a crucial role in identifying the defect species in the ZnO structure and distinguishing between intrinsic and extrinsic defects, and core and shell defects of ZnO. The main advantage of EPR spectroscopy is that it is sensitive to paramagnetic defects only. Thus, it makes it possible to accurately identify the defect source in the structure.

Fig.18 (a) below shows the EPR spectra of pure ZnO samples synthesized by the microwave-assisted method with microwave powers of 160 W, 320 W, and 800 W. (b) shows the integrated EPR spectra to have a better visualization of the intrinsic defect structure.
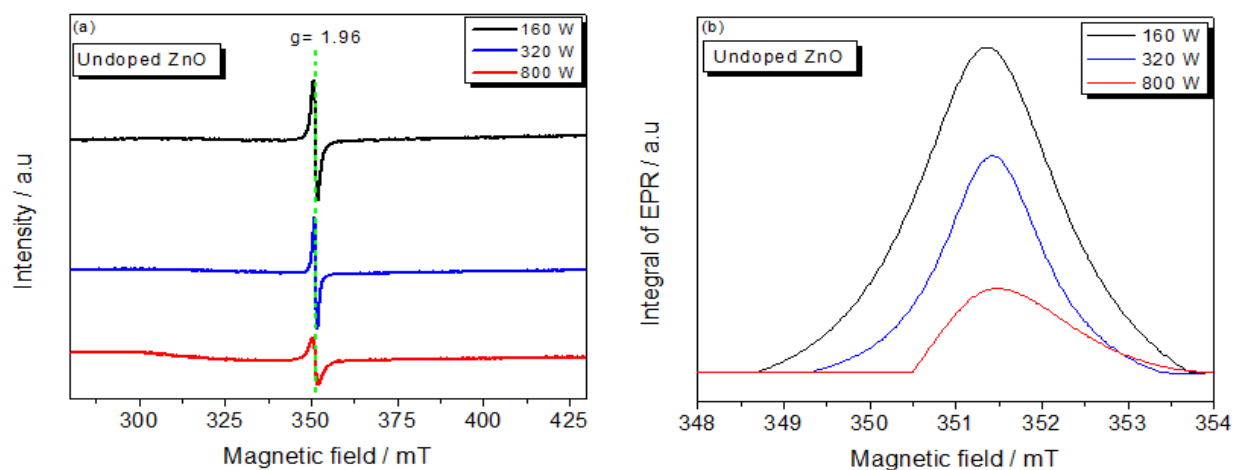
Figure 18: (a) EPR spectra of pure ZnO samples synthesized with varying microwave power outputs **(b)** Integrated EPR spectra.

The intrinsic defect structure of ZnO has been explained thoroughly in previous studies by Erdem *et al* [46]. ZnO has a unique defective structure that can be accurately detected by EPR spectroscopy. When the resonance condition is fulfilled (equation 8) and Zeeman splitting occurs, determining the g factor can give insight into the structure of the intrinsic defects. As per the explanation in ZnO properties, these defects might arise due to oxygen vacancy or interstitial, or zinc vacancy or interstitial. g value obtained from EPR spectra reveals the location of such defects. Surface or shell defects are associated with g = 2.002, and core or bulk defects are associated with g = 1.960 due to shielding of free electrons as shown in Fig.19 below.
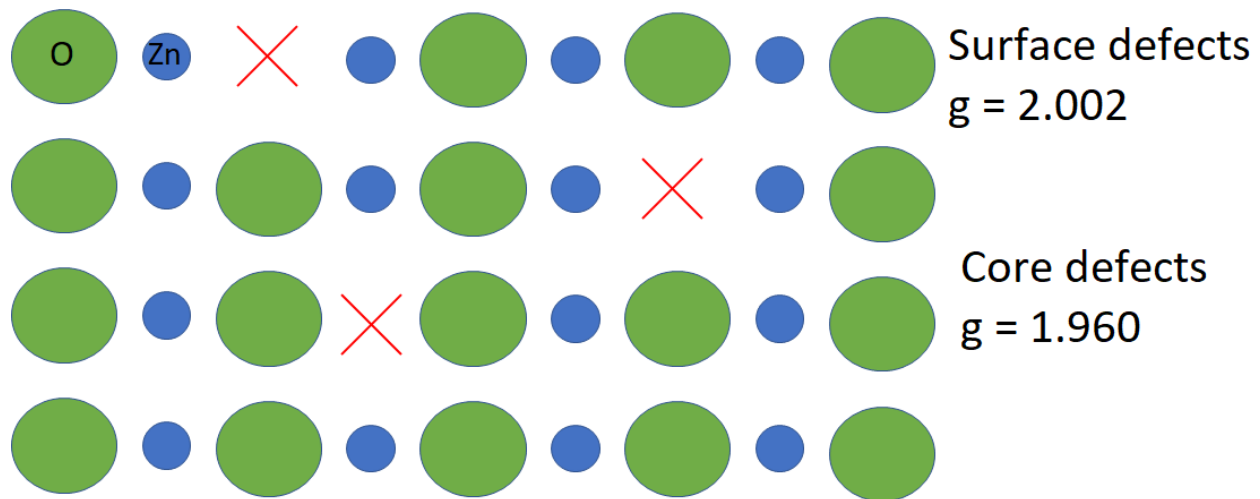
Figure 19: Surface and core defects of ZnO structure due to shielding of core signal.

Fig.18 (a) shows EPR signals around g = 1.960 and no major signals around g = 2.002 which indicates the presence of only core defects in the structure of pure ZnO samples. The intensity of these defects decreases from 160 W to 800 W as shown in Fig.18 (b). Thus, in addition to producing NWs with a higher AR, 160 W samples also show signals of a higher core defective structure [26, 47, 48].

The linewidth values were estimated by simulating the EPR spectra by using "Pepper" function of Easyspin in Matlab software [49]. Simulating EPR spectra provides great advantages such as understanding the parameters affecting the spectra, and providing means to accurately estimate the values of these parameters such as linewidth, g factor, and hyperfine structure tensor. Fig.20 below shows simulated and experimental EPR spectra of the undoped ZnO 160 W microwave power output sample. Table 9 shows the values of the g factor and linewidth of undoped ZnO samples with varying microwave power output.
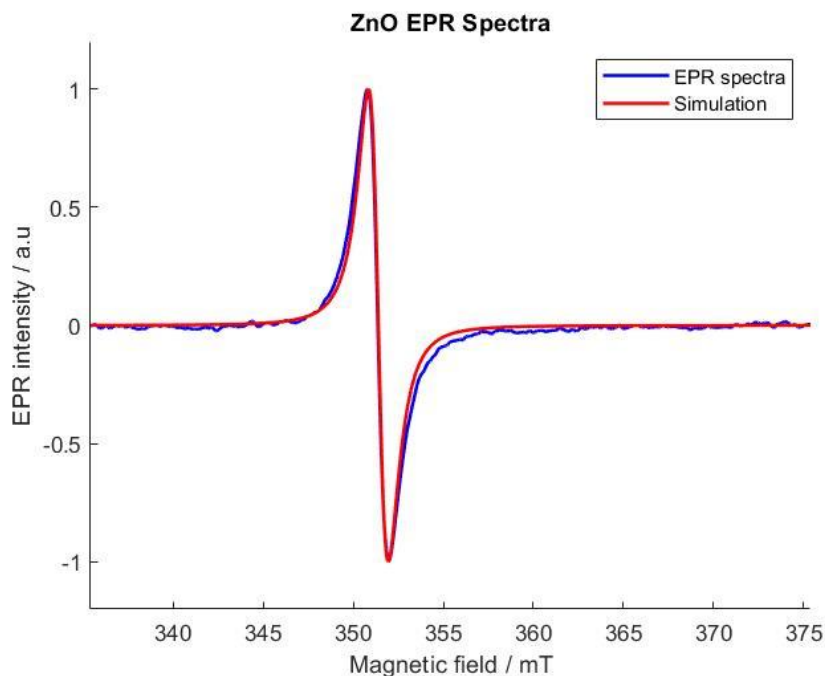
Figure 20: EPR data simulation of pure ZnO synthesized by the microwave-assisted hydrothermal method by using "pepper" function of Easyspin in Matlab.

Table 9: Linewidth and g factor obtained from EPR simulation.

Microwave power / W	g factor	ΔH **Linewidth / mT**
160	[1.962 1.962 1.962]	2
320	[1.962 1.962 1.962]	1.5
800	[1.962 1.962 1.962]	2.5

As can be observed from table 9 above, all the synthesized samples display isotropy in the g factor. Samples of 320 W show the smallest value of linewidth, which means they have the shortest relaxation time according to the formula:

$$\Delta H = \frac{1}{T_2} + \frac{1}{2T_1} \qquad (12)$$

Where ΔH: is the linewidth in mT.

T_2: is the spin-spin relaxation time in mT.

T_1: is the spin-lattice relaxation time in mT.

Usually, T_1 is larger than T_2, and the linewidth mainly depends on the spin-spin relaxation time T_2 [50]. Fig.21 below shows the EPR spectra of ball-milled pure ZnO samples as a function of increasing ball-milling time.
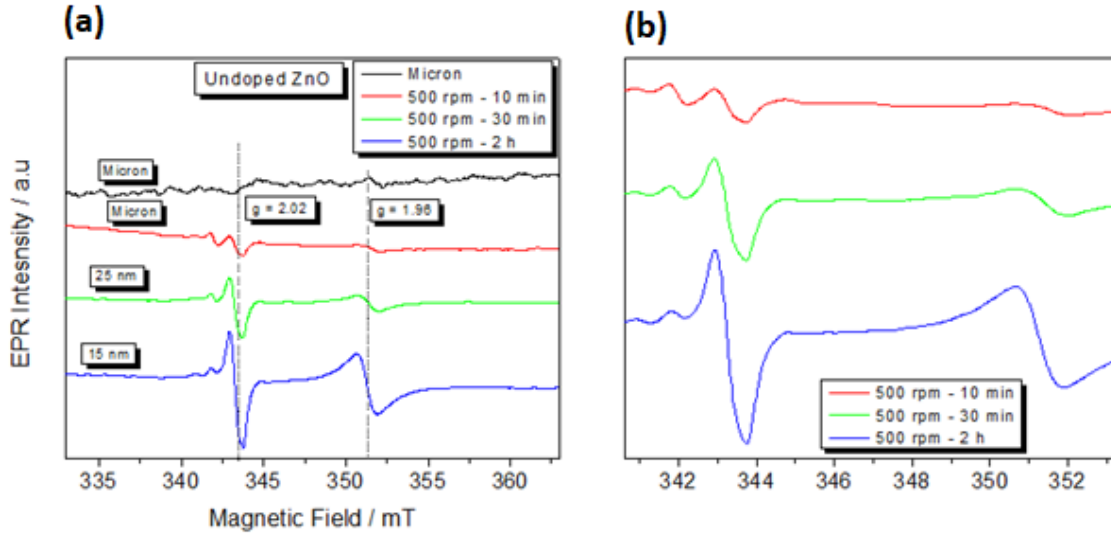
Figure 21: (a) EPR spectra of ball-milled pure ZnO samples as a function of ball-milling time (b) EPR peaks approaching isotropy.

As can be observed from Fig.21 (a) above, increasing the ball-milling time increases both signals of surface and core associated defects at $g = 2.02$ and $g = 1.96$ respectively. Surface signals are dominating as the milling time increases. As per the discussion in XRD section, increasing the milling time leads to a decrease in the average crystallite size, which introduces intrinsic defective structure into ZnO samples as can be displayed from the EPR spectra above. The main reason for the domination of surface defects is the increase of surface area to volume ratio as the average crystallite size decreases as can be seen in Fig.22 below.
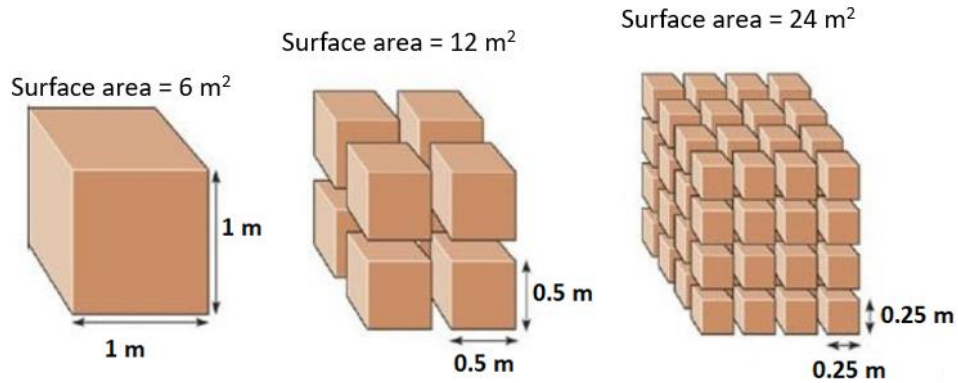
Figure 22: Surface area to volume ratio as a function of decreasing crystallite size (adapted from [51].

Another interesting observation from the EPR graph shown in Fig.21 (b), and simulating the samples by using the pepper function is the anisotropy of the g factor. It can be observed that increasing the ball milling time causes the g factor to approach isotropy as the milling time increases. In other words, as the samples' average crystallite size decreases, the g factor signals associated with core and surface defects tend to get closer to being isotropic. Fig.23 below shows the simulation of a pure ZnO sample ball-milled for 2 hours at 500 rpm milling speed.
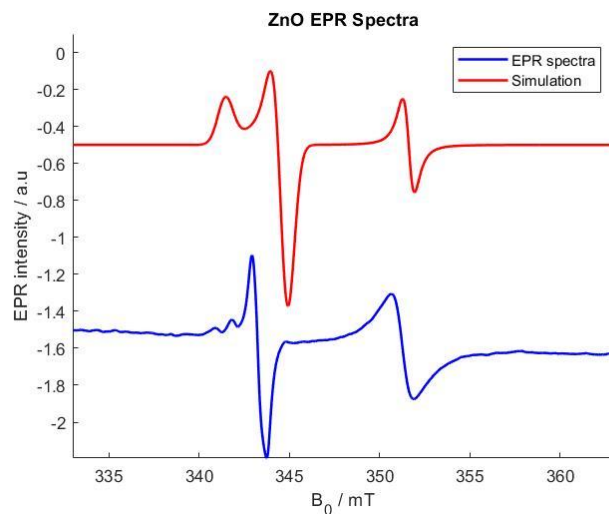
Figure 23: EPR data simulation of 2 hours ball-milled pure ZnO sample by using the "pepper" function.

Fig.24 below shows the EPR spectra of pure and Mn-doped ZnO NWs synthesized by the microwave-assisted hydrothermal method at (a) 160 W and (b) 800 W microwave power output.
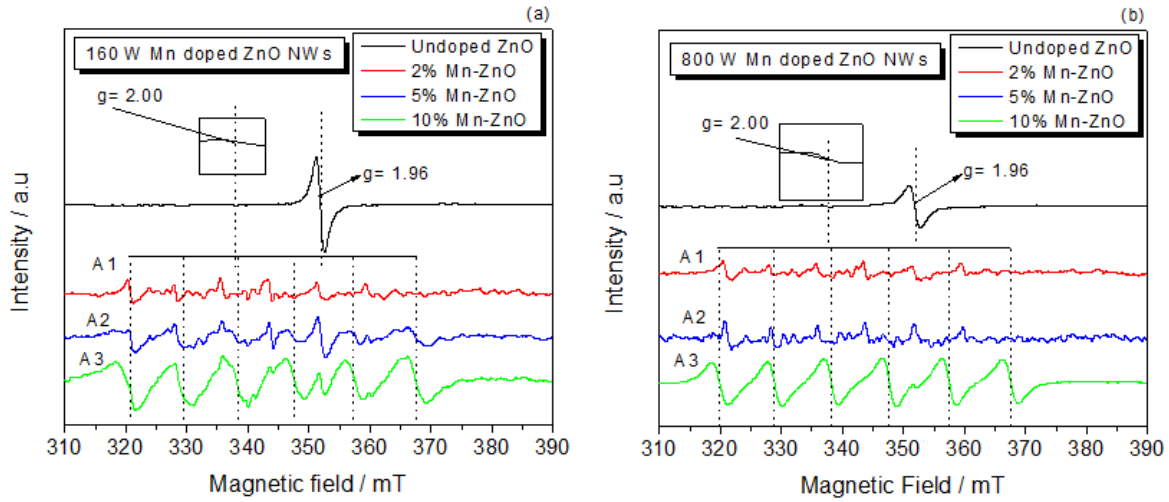
Figure 24: EPR spectra of pure and Mn-doped ZnO NWs synthesized with (a) 160 W microwave power and (b) 800 W microwave power.

As shown in Fig.24 above, Mn-doped ZnO samples show the typical sextet hyperfine line peaks associated with the incorporation of Mn^{+2} ions into the crystal structure of ZnO. Pure ZnO samples reflect only intrinsic defects, while Mn-doped ZnO samples reflect intrinsic and extrinsic defects [52-54], and EPR spectra show the difference clearly.

The EPR spectra of Mn-doped ZnO can be described by spin-hamiltonian resonance condition as follows [55, 56]:

$$\overrightarrow{H_s} = g_e \beta_e B_0 + SAI \qquad (13)$$

Where S: is the electronic spin operator.

A: is the hyperfine structure tensor in mT or MHz.

I: is the nuclear spin operator.

The difference between the resonance conditions at equations (8) and (13) is hyperfine structure SAI arising as a result of intrinsic structure defects due to Mn dopant. The hyperfine structure tensor can be visually calculated from the EPR spectra, indicated by A_1, A_2, and A_3 in Fig.24. However, for more accurate estimation, it is better to simulate the spectra by using the pepper function of easyspin and calculate the values of A tensor from the best fit. Fig.25 below shows the simulation of a 10%Mn-ZnO sample synthesized with 800 W microwave power, and table 10 shows calculated values of the hyperfine structure tensor both visually, and from the fitted spectra simulation.
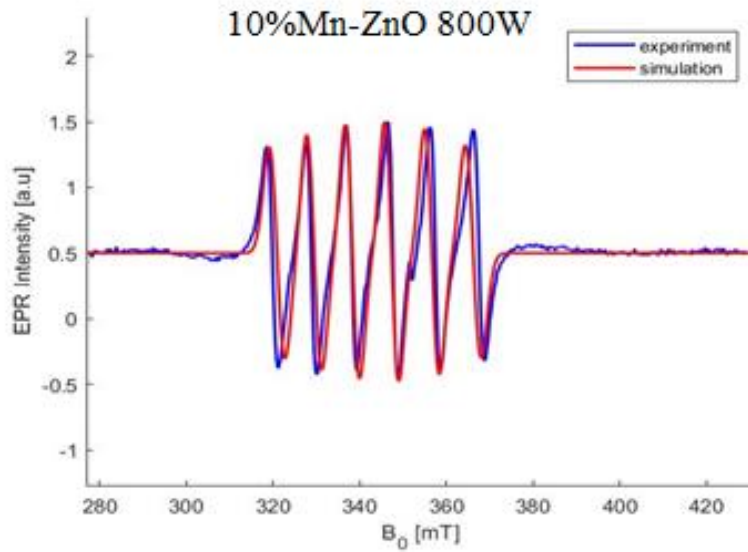
Figure 25: EPR data simulation of 10% Mn-ZnO NWs synthesized with 800 W microwave power.

Table 10: calculations of the hyperfine tensor A from EPR spectra and EPR simulation.

Hyperfine structure tensor	160 W visual calculation (mT)	160 W simulation calculation (MHz)	800 W visual calculation (mT)	800 W simulation calculation (MHz)
A_1	7.6	[226 221 220]	7.4	[219 223 220]
A_2	7.8	[222 239 222]	7.8	[222 239 222]
A_3	8.8	[266 265 265]	8.5	[261 262 261]

Fig. 26 below shows the EPR spectra of the 10%Mn-ZnO sample before and after heat treatment.
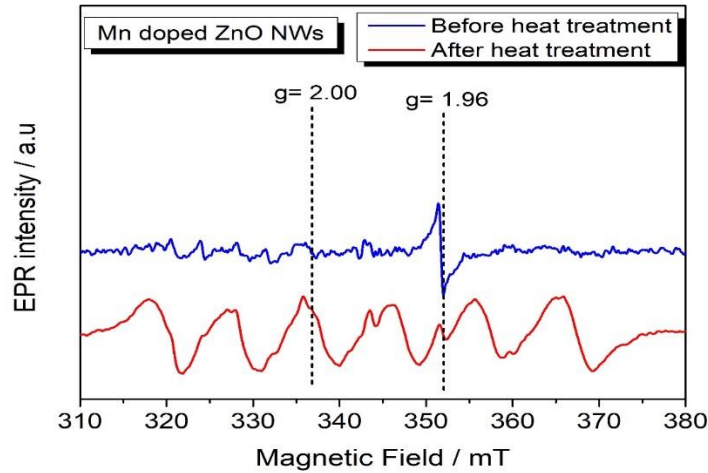
Figure 26: EPR spectra of 10%Mn-ZnO sample before and after heat treatment.

Fig.26 above displays two important facts. The first one is the necessity of the heat treatment process for the synthesized samples. As can be noticed, samples without heat treatment only display the EPR peaks associated with the intrinsic defect structure of ZnO, and do not show any sign of the extrinsic defect structure even though Mn is present in the structure. This analysis shows that the energy supplied by the microwave alone is not enough to fully incorporate Mn ions into the structure of ZnO. However, after supplying heat energy in the heat treatment process, the sextet hyperfine peaks associated with Mn ions incorporation into ZnO structure can be observed. The other fact is the crucial role of EPR spectra in the synthesized samples. These results are only observed by conducting EPR spectroscopy, as they can not be observed as clearly by other characterization techniques. Since the temperature of the microwave is constant for both 160 W and 800 W around 85-90 °C, and 800 W samples are subject to more energy than 160 W samples, it is natural that the heat treatment process of 160 W samples must be conducted at higher temperatures or slightly higher times than 800 W samples.

Table 11 below shows the heat treatment process optimization for the synthesized samples.

Table 11: Heat treatment process optimization for the synthesized samples.

Mn (mol%)	Microwave power (W)	Time in the microwave (min)	Heat treatment temperature (^oC)	Heat treatment time (hours)
2	800	15	450	3.5
5	800	15	400	3.5
10	800	15	200	2
2	160	15	500	3.5
5	160	15	450	3.5
10	160	15	200	2

5.4.PL analysis:

The optical properties of the synthesized pure and Mn-doped ZnO samples were analyzed by PL spectroscopy. PL is sensitive to all types of defects, unlike EPR which is only sensitive to paramagnetic defects. Thus, PL spectroscopy can provide great advantages in detecting structural defects.

Fig.27 below shows the PL spectra of pure ZnO samples synthesized with varying microwave powers and the deconvolution of the peaks displaying the different emission regions.
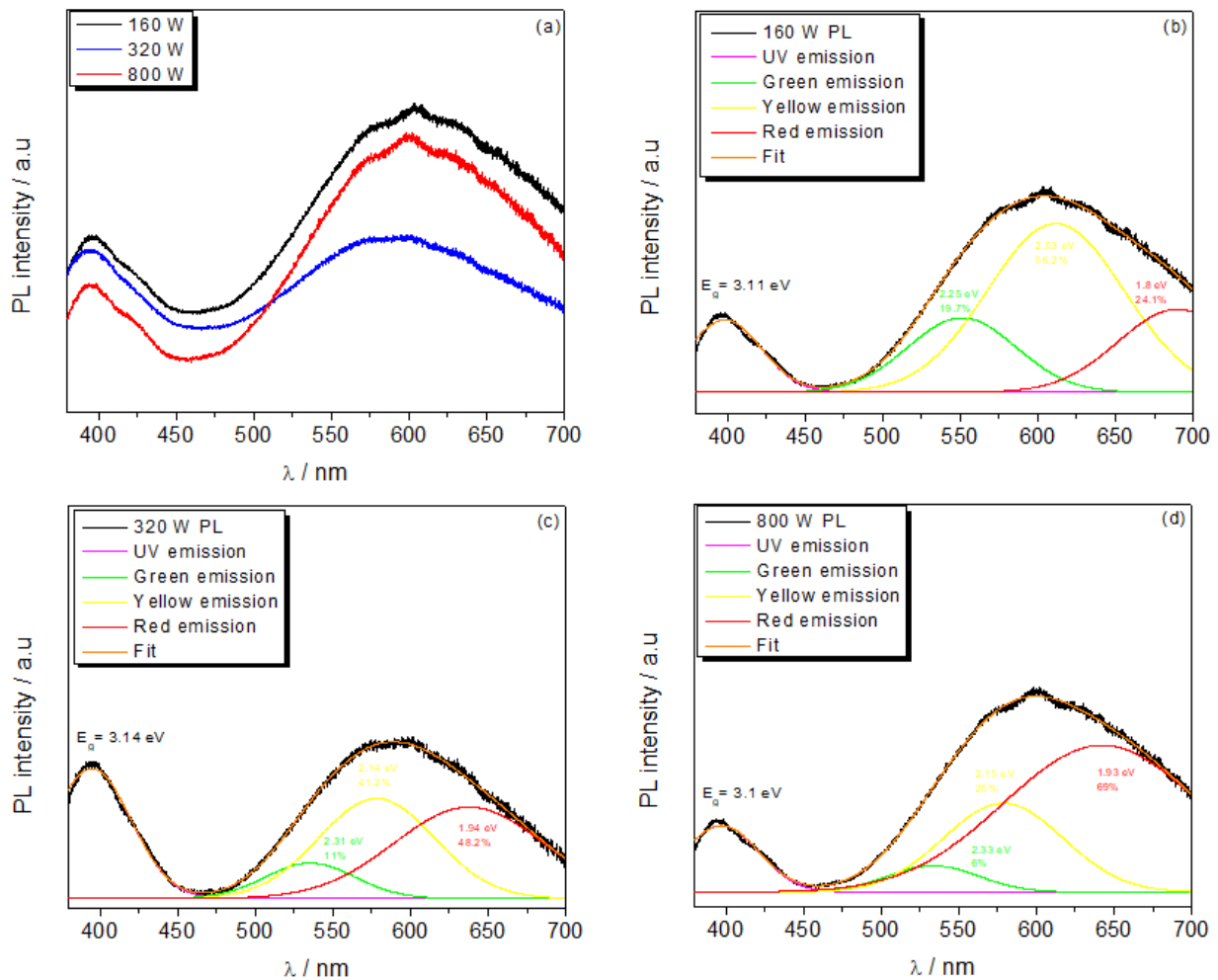
Figure 27: (a) PL spectra of pure ZnO samples synthesized via the microwave-assisted hydrothermal method with varying microwave powers. (b) Deconvolution of 160 W PL. (c) Deconvolution of 320 W PL. (d) Deconvolution of 800 W PL.

As can be seen from Fig.27, samples synthesized with varying microwave powers all display a defective structure, and these results were expected since the samples lie in the nano-scale. PL results are in good agreement with previously discussed results of XRD, SEM, and EPR. The first peak at around 380-390 nm is associated with the bandgap energy of the samples, and the wide peak in the visible light range is associated with the defective structure of ZnO [25, 27, 46, 57].

The bandgap energy can be calculated with high accuracy by using:

$$E_g = \frac{hc}{\lambda} = \frac{1240}{\lambda} \qquad (14)$$

Where: E_g is the bandgap energy in eV.

h is Planck's constant in eV s.

c is the speed of light in m/s.

λ is the wavelength in nm.

Bandgap energies for all samples are estimated at around 3.1 eV, and these results are in good agreement with the typical E_g value of ZnO. On the other hand, deconvolution of the emission peak in the visible range displays interesting results. A decrease in the green and yellow emissions and an increase in the red emission can be noticed as the microwave power increases. Several studies associated the green and yellow emissions with oxygen vacancies V_o, Zinc vacancies V_{Zn}, donor-acceptor pairs, and red emissions to oxygen interstitials O_i and vacancies V_O [25, 27, 46, 58]. The reduction in red emission is also associated with the reduction of particle size, and these results are in good agreement with previous discussions in XRD and TEM regarding average crystallite and particle size calculations.

Fig.28 below shows the PL spectra of ball-milled Sigma Aldrich ZnO samples as a function of milling time.
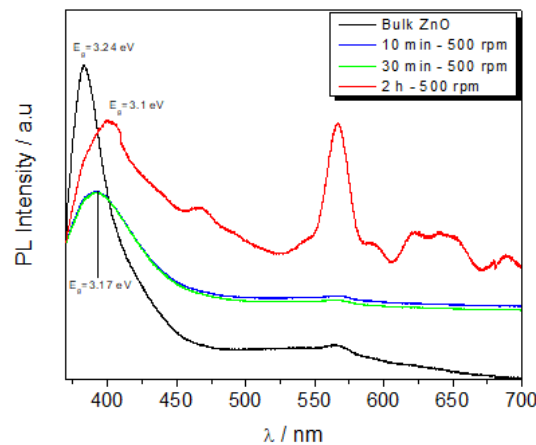
Figure 28: PL spectra of ball-milled ZnO samples as a function of milling time.

Fig.28 above shows the relation between ball-milling (reducing particle size) and the PL spectra of ZnO samples. A reduction of bandgap energy can be observed as the milling time increase, from 3.24 eV for the bulk sample to 3.1 eV of the nano-scaled sample after 2 hours of milling. Bulk samples reveal only one major peak associated with the bandgap energy of ZnO in the UV region, while nano-scaled samples reveal additional peaks in the visible light region associated with the aforementioned defect species [25, 46]. A correlation between PL, EPR, and XRD results can be made to further understand the effect of the defective structure of ZnO. It is worth noting here that PL results reveal that ball-milled samples at 10 minutes and 30 minutes have not reached the nano-scale yet. Thus, the results in Table 6 for these samples are questionable, but for 2 hours the results in Table 6 are certainly accurate since PL spectra reveal the samples lie on the nano-scale.

Fig.29 below shows the PL spectra of pure and Mn-doped ZnO samples synthesized with 160 W and 800 W microwave powers.
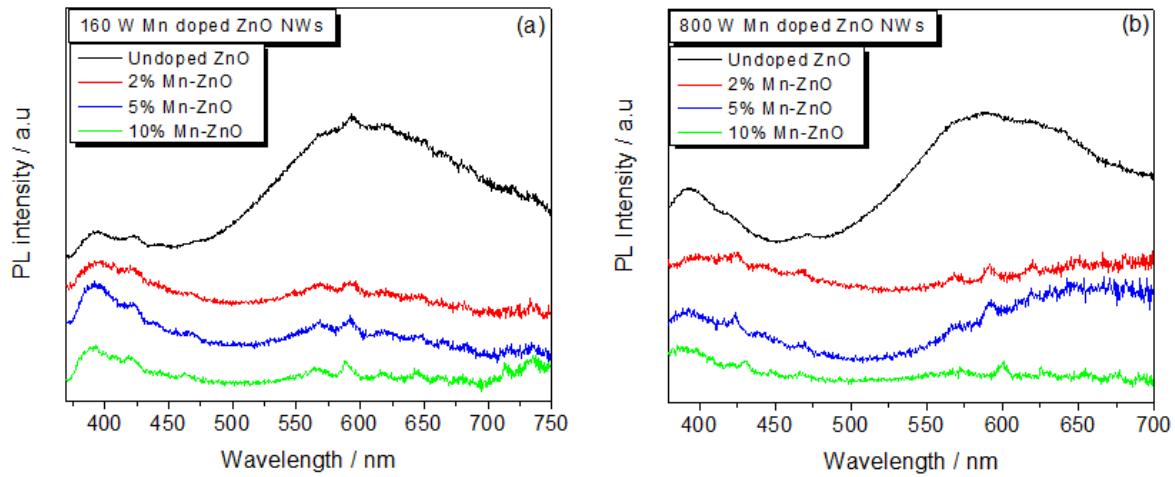
Figure 29: PL spectra of pure and Mn-doped ZnO samples synthesized with (a) 160 W and (b) 800 W microwave powers.

As can be observed from Fig.29, doping ZnO with Mn ions diminishes and flattens the peaks in the visible light range. In this case, extrinsic defects introduced into the structure of ZnO seem to alter the intrinsic defects and reduce their effect as Mn ions fill zinc vacancies V_{Zn} [25, 58].

5.5. Piezoelectric coefficient d$_{33}$ measurement:

To measure the piezoelectric coefficient d$_{33}$ of the ZnO samples, they should be grown on a substrate first. A range of flexible or hard substrates can be selected, such as polyethylene terephthalate (PET), polydimethylsiloxane (PDMS), glass substrates based on silicon, and many others. The substrate is cleaned in an ultrasonic bath of DI water, and ethanol for 15 minutes each. After cleaning the substrates, a seeding layer solution is prepared whose main function is to promote the growth of ZnO NWs on the substrate in a vertically aligned manner [59, 60]. A 20 mM solution of zinc acetate dihydrate in ethanol, aged for 24 hours is used as the seeding layer. The seeding layer is spread on the substrate and spin-coated at 1500 rpm for 30 seconds thrice, then dried in the oven at 90 ºC for 10 minutes. The whole process of coating and drying is repeated thrice to ensure the appropriate thickness of the seeding layer on the substrate. Finally, the growth of ZnO NWs is achieved by repeating the same aforementioned process in the experimental section, and by placing the substrate face-up at the bottom of the precursor solution. Fig.30 below shows a schematic of the effect of the seeding layer, and the images of substrates prepared in the lab.
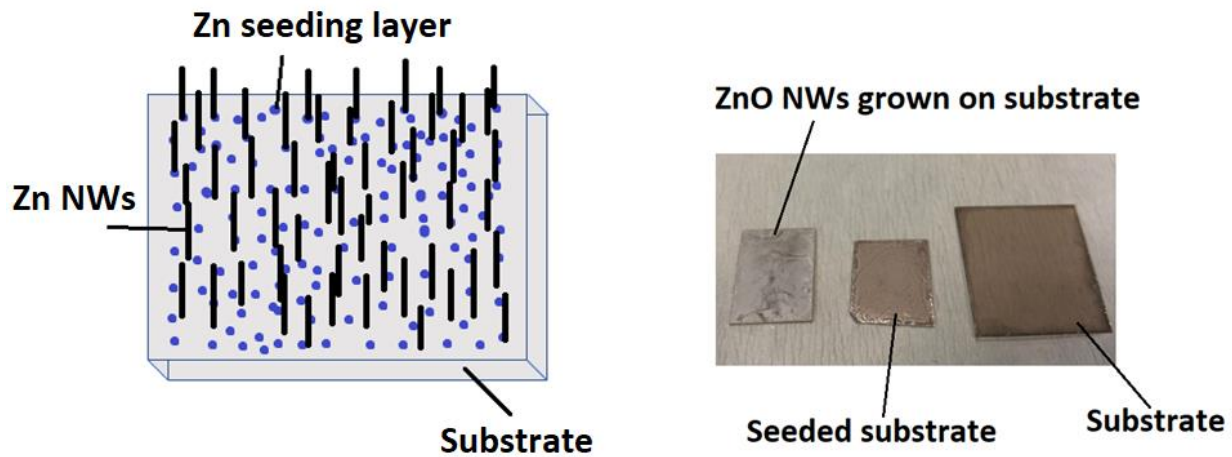
Figure 30: Schematic of the effect of the seeding layer, and ZnO NWs growth on a substrate in the lab.

Fig.31 below shows the main components of the D33PZO1 measurement device.

Figure 31: Main components of D33PZO1 measurement device.

The substrate with grown ZnO NWs is placed between the two knobs, and tightened until the static force reading on the measurement device is 250 N. The sample holder applies a dynamic force on the substrate, and it is connected to the measurement device. The measurement device analysis the substrate's response to the applied dynamic force and gives a direct measurement of the d_{33} value. Table 12 below shows the results of d_{33} measurements for different samples.

Table 12: Measurement of d_{33} value for different samples.

Sample	d33 value (2% error)/pC/N
ZnO with 160 W	22
ZnO with 320 W	14
ZnO with 800 W	11
5% MnZnO with 800 W	10

As can be seen from Table 12 above, ZnO NWs synthesized at 160 W shows the highest reading for d_{33} coefficient, and these results are in good agreement with our spectroscopic analysis since they revealed the highest AR among the samples. The measured values show promising results compared to the average value of d_{33} in the range 10-15 pC/N.

As for Mn-doped samples, not much of a difference is measured. Mn-doped sample's d_{33} is related to the ease of stressing the nanowire with the presence of Mn dopant [61].

6. Conclusions:

This thesis provides some insights into the evergrowing research of ZnO synthesis, properties, and defective structure. ZnO NWs have a promising potential for piezoelectric nanogenerator applications owing to their attractive properties such as being a bio-safe and biodegradable materials, and high piezoelectric coefficient d_{33}. Amongst the wide range of synthesis techniques, the microwave-assisted hydrothermal technique provides critical advantages including simplicity, low cost, and rapidness. ZnO NWs have been successfully synthesized by using this process. The effect of microwave power on the quality of produced ZnO NWs has been studied by analyzing the intrinsic defective structure of the products. The extrinsic defective structure has been studied by successfully doping ZnO NWs with TMI such as Mn, which also widens the applications of ZnO NWs to include DMS materials. The AR of the product has been controlled successfully by varying the microwave power levels during the synthesis process, and high values of AR up to 22.6 were obtained by using low microwave power of 160 W.

XRD provided an analysis of the crystalline structure of the produced ZnO NWs, and the average crystallite size has been calculated successfully by using different techniques such as Scherrer's equation and W-H Plots. SEM images revealed the nanostructure and morphology of the synthesized ZnO NWs and revealed the effect of Mn-dopant on the morphology. The average particle size has been calculated successfully by analyzing the SEM images. EPR analysis provided an accurate analysis of the intrinsic and extrinsic defective structure of ZnO, and the simulation of EPR by using the pepper function in MATLAB provided a clear understanding of the origin of the defective structure. The optical properties have been analyzed by PL spectroscopy, which provided means of accurately calculating the bandgap energy of different synthesized samples, understanding the core-shell model from the optical point of view, and analyzing the defects in the visible light emission range. To fully grasp the boundary between bulk and nano properties of ZnO, a separate analysis has been implemented for all of the aforementioned techniques by analyzing samples processed by ball-milling, for up to 2 hours which yielded nano-scaled ZnO (15 nm) from bulk ZnO (few μm). A correlation between the various methods has been successfully proven, and the results were complementary to each other.

Finally, ZnO NWs have been successfully grown on a flexible substrate after applying a convenient Zn seeding layer, and promising results of d_{33} coefficient up to 22 pC/N compared to the typical values of 10-15 pC/N for ZnO have been measured.

7. References:

1. IEA, *NetZeroby2050-ARoadmapfortheGlobalEnergySector.* 2020.
2. Wang, Z.L.S., Jinhui, *Piezoelectric nanogenerators based on zinc oxide nanowire arrays.* Science (New York, N.Y.), 2006. **312**(5771).
3. Yang, R., et al., *Power generation with laterally packaged piezoelectric fine wires.* Nature Nanotechnology, 2009. **4**(1): p. 34-39.
4. Wang, Z.L.Z., Guang; Yang, Ya; Wang, Sihong; Pan, Caofeng, *Progress in nanogenerators for portable electronics.* Materials today, 2012. **15**(12).
5. Di Liu; Yin, X.G., Hengyu; Zhou, Linglin; Li, Xinyuan; Zhang, Chunlei; Wang, Jie; Wang, Zhong Lin, *A constant current triboelectric nanogenerator arising from electrostatic breakdown.* Science advances, 2019. **5**(4).
6. Yang, Y.W., Sihong; Zhang, Yan; Wang, Zhong Lin, *Pyroelectric nanogenerators for driving wireless sensors.* Nano Letters, 2012. **12**(12).
7. Al-Ruqeishi, M.S., et al., *Piezoelectric nanogenerator based on ZnO nanorods.* Arabian Journal of Chemistry, 2019. **12**(8): p. 5173-5179.
8. Opoku, C., et al., *Fabrication of ZnO Nanowire Based Piezoelectric Generators and Related Structures.* Physics Procedia, 2015. **70**: p. 858-862.
9. Zhang, Y., et al., *Synthesis, Characterization, and Applications of ZnO Nanowires.* Journal of Nanomaterials, 2012. **2012**: p. 624520.
10. Uchino, K., *Chapter 1 - The Development of Piezoelectric Materials and the New Perspective*, in *Advanced Piezoelectric Materials (Second Edition)*, K. Uchino, Editor. 2017, Woodhead Publishing. p. 1-92.
11. Yang, C.E., *What is the Piezoelectric Effect?* ElectronicDeisn, 2016.
12. Huang, H.-H., et al., *Epitaxial PbZrxTi1−xO3 Ferroelectric Bilayers with Giant Electromechanical Properties.* Advanced Materials Interfaces, 2015. **2**.
13. Mends, F., *What Are Piezoelectric Materials?*
14. Leighton, G. and Z. Huang, *Accurate measurement of the piezoelectric coefficient of thin films by eliminating the substrate bending effect using spatial scanning laser vibrometry.* Smart Materials & Structures - SMART MATER STRUCT, 2010. **19**.
15. Justeau, C., et al., *A Comparative Study on the Effects of Au, ZnO and AZO Seed Layers on the Performance of ZnO Nanowire-Based Piezoelectric Nanogenerators.* Materials (Basel), 2019. **12**(16).
16. Wang, Z.L. and J. Song, *Piezoelectric Nanogenerators Based on Zinc Oxide Nanowire Arrays.* Science, 2006. **312**(5771): p. 242-246.
17. Wang, Z.L., et al., *Progress in nanogenerators for portable electronics.* Materials Today, 2012. **15**(12): p. 532-543.
18. Zhu, G., et al., *Flexible High-Output Nanogenerator Based on Lateral ZnO Nanowire Array.* Nano Letters, 2010. **10**(8): p. 3151-3155.
19. Kammel, R.S. and R.S. Sabry, *Effects of the aspect ratio of ZnO nanorods on the performance of piezoelectric nanogenerators.* Journal of Science: Advanced Materials and Devices, 2019. **4**(3): p. 420-424.
20. Sharma, D.K., et al., *A review on ZnO: Fundamental properties and applications.* Materials Today: Proceedings, 2022. **49**: p. 3028-3035.
21. Project, T.M., *ZnO Wurtzite Structure.*
22. Özgür, U.m., D. Hofstetter, and H. Morkoç, *ZnO Devices and Applications: A Review of Current Status and Future Prospects.* Proceedings of the IEEE, 2010. **98**: p. 1255-1268.

23. Willander, M., *Optical Properties of and Optical Devices from ZnO-Based Nanostructures*, in *Zinc Oxide Nanostructures*, M. Willander, Editor. 2013, Jenny Stanford Publishing.

24. Kaftelen, H., et al., *EPR and photoluminescence spectroscopy studies on the defect structure of ZnO nanocrystals.* Physical Review B, 2012. **86**(1): p. 014113.

25. Aleinawi, M.H., et al., *Spectroscopic Probing Of Mn-Doped ZnO Nanowires Synthesized via a Microwave-Assisted Route.* The Journal of Physical Chemistry C, 2022. **126**(8): p. 4229-4240.

26. Schneider, J.J., et al., *Synthesis, Characterization, Defect Chemistry, and FET Properties of Microwave-Derived Nanoscaled Zinc Oxide.* Chemistry of Materials, 2010. **22**(7): p. 2203-2212.

27. Erdem, E., *Microwave power, temperature, atmospheric and light dependence of intrinsic defects in ZnO nanoparticles: A study of electron paramagnetic resonance (EPR) spectroscopy.* Journal of Alloys and Compounds, 2014. **605**: p. 34-44.

28. Parashar, S.K.S., et al., *Investigation of intrinsic defects in core-shell structured ZnO nanocrystals.* Journal of Applied Physics, 2012. **111**(11): p. 113712.

29. Hu, G., et al., *Properties of p-type and n-type ZnO influenced by P concentration.* Applied Physics Letters, 2006. **89**(25): p. 251102.

30. Guruvammal, D., S. Selvaraj, and S. Meenakshi Sundar, *Structural, optical and magnetic properties of Co doped ZnO DMS nanoparticles by microwave irradiation method.* Journal of Magnetism and Magnetic Materials, 2018. **452**: p. 335-342.

31. Ruf, T., et al., *Competing effects between intrinsic and extrinsic defects in pure and Mn-doped ZnO nanocrystals.* Journal of Nanoparticle Research, 2016. **18**: p. 1-11.

32. Bagga, S., J. Akhtar, and S. Mishra, *Synthesis and applications of ZnO nanowire: A review*. Vol. 1989. 2018. 020004.

33. Zhao, X., et al., *Synthesis of Monodispersedly Sized ZnO Nanowires from Randomly Sized Seeds.* Nano Letters, 2020. **20**(1): p. 599-605.

34. Xu, S. and Z.L. Wang, *One-dimensional ZnO nanostructures: Solution growth and functional properties.* Nano Research, 2011. **4**(11): p. 1013-1098.

35. Govender, K., et al., *Understanding the factors that govern the deposition and morphology of thin films of ZnO from aqueous solution.* Journal of Materials Chemistry, 2004. **14**(16): p. 2575-2591.

36. Ku, C.-H., et al., *Wet-Chemical Route to ZnO Nanowire-Layered Basic Zinc Acetate/ZnO Nanoparticle Composite Film.* Crystal Growth & Design, 2008. **8**(1): p. 283-290.

37. Parize, R., et al., *Effects of Hexamethylenetetramine on the Nucleation and Radial Growth of ZnO Nanowires by Chemical Bath Deposition.* The Journal of Physical Chemistry C, 2016. **120**(9): p. 5242-5250.

38. Shim, J.B., *Rapid Hydrothermal Synthesis of Zinc Oxide Nanowires by Annealing Methods on Seed Layers.* Journal of Nanomaterials, 2011. **2011**: p. 582764.

39. Tian, J., et al., *Improved seedless hydrothermal synthesis of dense and ultralong ZnO nanowires.* Nanotechnology, 2011. **22**: p. 245601.

40. Mohammadi, E., et al., *Hierarchical and Complex ZnO Nanostructures by Microwave-Assisted Synthesis: Morphologies, Growth Mechanism and Classification.* Critical Reviews in Solid State and Materials Sciences, 2018. **43**(6): p. 475-541.

41. Malajovich, I., et al., *Persistent sourcing of coherent spins for multifunctional semiconductor spintronics.* Nature, 2001. **411**(6839): p. 770-2.

42. Prabhu, Y., et al., *X-Ray Analysis by Williamson-Hall and Size-Strain Plot Methods of ZnO Nanoparticles with Fuel Variation.* World Journal of Nano Science and Engineering, 2014. **04**: p. 21-28.

43. Ahmed, S.A., *Structural, optical, and magnetic properties of Mn-doped ZnO samples.* Results in Physics, 2017. **7**: p. 604-610.

44.   Iqbal, T., et al., *Influence of Manganese on structural, dielectric and magnetic properties of ZnO nanoparticles.* Digest Journal of Nanomaterials and Biostructures, 2016. **11**: p. 899-908.

45.   Toloman, D., et al., *Evidence by EPR of ferromagnetic phase in Mn-doped ZnO nanoparticles annealed at different temperatures.* JOURNAL OF ALLOYS AND COMPOUNDS, 2013. **551**: p. 502-507.

46.   Nadupalli, S., et al., *About defect phenomena in ZnO nanocrystals.* Nanoscale, 2021. **13**.

47.   Schneider, J., et al., *Zinc oxide derived from single source precursor chemistry under chimie douce conditions: Formation pathway, defect chemistry and possible applications in thin film printing.* Journal of Materials Chemistry, 2009. **19**.

48.   Jakes, P. and E. Erdem, *Finite size effects in ZnO nanoparticles: An electron paramagnetic resonance (EPR) analysis.* physica status solidi (RRL) – Rapid Research Letters, 2011. **5**(2): p. 56-58.

49.   U.S. National Science Foundation, t.U.S.N.I.o.H., and the Swiss National Science Foundation., *Easyspin.* 2022. **5.2.35**.

50.   Lindon, J.C.T.G.E.K.D.W., *Encyclopedia of spectroscopy and spectrometry.* 2016.

51.   Agista, M., *A Literature Review and Transport Modelling of Nanoparticles for Enhanced Oil Recovery*. 2017.

52.   Reddy, A.J., et al., *EPR and photoluminescence studies of ZnO:Mn nanophosphors prepared by solution combustion route.* Spectrochimica Acta Part A: Molecular and Biomolecular Spectroscopy, 2011. **79**(3): p. 476-480.

53.   Acikgoz, M., et al., *Local coordination of Fe3+ in ZnO nanoparticles: Multi-frequency electron paramagnetic resonance (EPR) and Newman superposition model analysis.* Journal of physics. Condensed matter : an Institute of Physics journal, 2014. **26**: p. 155803.

54.   Yüksel Price, B., et al., *Effects of MnO doping on the electronic properties of zinc oxide: 406 GHz electron paramagnetic resonance spectroscopy and Newman superposition model analysis.* Journal of Applied Physics, 2015. **118**.

55.   Ankiewicz, A., et al., *Electron paramagnetic resonance in transition metal-doped ZnO nanowires.* Journal of Applied Physics, 2007. **101**: p. 024324-024324.

56.   Zhou, H., et al., *Magnetic resonance investigation of Mn2+ in ZnO nanocrystals.* Journal of Applied Physics, 2003. **94**(3): p. 1965-1968.

57.   Erdem, E., *Microwave power, temperature, atmospheric and light dependence of intrinsic defects in ZnO nanoparticles: A study of electron paramagnetic resonance (EPR) spectroscopy.* Journal of Alloys and Compounds, 2014. **605**: p. 34–44.

58.   Ahn, C., et al., *A comparative analysis of deep level emission in ZnO layers deposited by various methods.* Journal of Applied Physics, 2009. **105**: p. 013502-013502.

59.   Semenova, A., et al., *Formation of ZnO nanorods on seed layers for piezoelectric nanogenerators.* Journal of Physics: Conference Series, 2017. **917**: p. 032022.

60.   Song, J. and S. Lim, *Effect of Seed Layer on the Growth of ZnO Nanorods.* Journal of Physical Chemistry C - J PHYS CHEM C, 2006. **111**.

61.   Vladut, C., et al., *Optical and Piezoelectric Properties of Mn-Doped ZnO Films Deposited by Sol-Gel and Hydrothermal Methods.* Journal of Nanomaterials, 2019. **2019**: p. 1-12.